AGU PUBLICATIONS

JGR

Journal of Geophysical Research: Atmospheres

RESEARCH ARTICLE
10.1002/2015JD023792

Key Points:
- Transatlantic dust transport is simulated with a global chemistry climate model
- Eulerian and Lagrangian diagnostics reveal main features of the dust transport
- Main source regions are located in Algeria, Mali, and Mauritania

Correspondence to:
G. Gläser,
gregor.glaeser@kit.edu

Citation:
Gläser, G., H. Wernli, A. Kerkweg, and F. Teubler (2015), The transatlantic dust transport from North Africa to the Americas—Its characteristics and source regions, *J. Geophys. Res. Atmos.*, *120*, 11,231–11,252, doi:10.1002/2015JD023792.

Received 12 JUN 2015
Accepted 4 OCT 2015
Accepted article online 7 OCT 2015
Corrected 25 JAN 2016

This article was corrected on 25 JAN 2016. See the end of the full text for details.

©2015. American Geophysical Union. All Rights Reserved.

The transatlantic dust transport from North Africa to the Americas—Its characteristics and source regions

Gregor Gläser[1,2], Heini Wernli[3], Astrid Kerkweg[1], and Franziska Teubler[1]

[1]Institute for Atmospheric Physics, University of Mainz, Mainz, Germany, [2]Institute of Meteorology and Climate Research—Troposphere Research, Karlsruhe Institute of Technology, Karlsruhe, Germany, [3]Institute for Atmosphere and Climate Science, ETH Zurich, Zurich, Switzerland

Abstract Transport of Saharan dust over the Atlantic to the Americas is a relevant process since dust is a nutrient for marine and terrestrial ecosystems. It is therefore important to better quantify the frequency and amount of transatlantic dust transport, its preferred altitude and duration, and the regions of dust origin. This study uses a novel combination of Eulerian and Lagrangian diagnostics, applied to a previously validated 5 year simulation of the fifth generation European Centre for Medium Range Weather Forecast-Hamburg-model (ECHAM5)/Modular Earth Submodel System (MESSy) Atmospheric Chemistry model, to quantify these dust transport characteristics and their seasonal variations. Results confirm the previously found preferred transatlantic dust pathways: in boreal winter and spring, African dust is mainly transported below 800 hPa toward South America, whereas in summer and autumn the preferred pathway is to the Caribbean and occurs in a layer up to 500 hPa. The averaged transport duration from dust emission to deposition is 10 days in winter for deposition in the Amazon region and almost 12 days in summer for deposition in the Caribbean. These estimates were obtained by combining correlation analyses of Eulerian dust fluxes and trajectory calculations. The latter were also essential to identify the main source regions of transatlantic dust transport, which were found in all seasons in northwestern Africa (Algeria, Mali, and Mauritania) but not farther east, e.g., in the Bodélé Depression. A specific Lagrangian analysis for this dust emission hot spot suggests that wet deposition associated with the Intertropical Convergence Zone in winter and the African monsoon in summer inhibits Bodélé dust to leave the African continent.

1. Introduction

First indications of Saharan dust reaching the Americas were reported already in the 1950s by *Junge* [1956]. Continuous dust measurements in Barbados exist since 1965 [*Prospero and Nees*, 1977], and other stations in the tropical and subtropical Americas followed in the 1970s, e.g., Miami, Florida, USA in 1974 [*Prospero*, 1999] and Cayenne, French Guiana in 1979 [*Péwé*, 1981]. Efforts to understand the characteristics of the transport have also been made since the early 1970s [*Prospero and Carlson*, 1970; *Carlson and Prospero*, 1972]. Today, African dust is known to be an important nutrient for the Amazon rainforest [e.g., *Swap et al.*, 1992; *Yu et al.*, 2015] and other marine and terrestrial ecosystems [e.g., *Mahowald et al.*, 2005; *Wang et al.*, 2012; *Gross et al.*, 2015]. Saharan dust directly and indirectly affects global and regional climate by influencing the radiation budget [*Mahowald et al.*, 2010; *DeFlorio et al.*, 2014] and potentially impacts the frequency of tropical cyclones and hurricanes [*Evan et al.*, 2006; *Bretl et al.*, 2015]. It is also an important source of ice nuclei in the Amazon Basin during the wet season [*Prenni et al.*, 2009].

These effects on ecosystems and weather in South America, the Caribbean, and the Atlantic Ocean necessitate detailed analyses of the transport characteristics of Saharan dust. In order to quantitatively estimate the impact of the dust, the following aspects need to be considered: (i) the frequency and amount of dust transport, (ii) the horizontal and vertical distribution and the duration of the transport, (iii) the specific regions of origin and chemical composition of the dust, and (iv) the seasonal variations of these aspects.

Prior to the atmospheric transport, dust needs to be emitted from the surface. Various emission mechanisms in different seasons and on different spatial scales have been identified, as described by *Knippertz and Todd* [2012]. Several studies analyzed the large-scale transport patterns and their fundamental seasonal variations [e.g., *Moulin et al.*, 1997; *Doherty et al.*, 2012, 2014]. In Northern Hemispheric (NH) winter, the Harmattan carries Saharan dust in western and southwestern directions within the trade wind layer, i.e., below 1.5–3 km

[*Schepanski et al.*, 2009]. The southern position of the Intertropical Convergence Zone (ITCZ) allows the transatlantic transport to reach the South American continent. Higher insolation and the northward shift of the ITCZ during NH summer cause a deeper boundary layer over Africa, leading to higher upward transport of dust by turbulent mixing in the convective boundary layer. The Harmattan blows this dust-laden air toward denser air masses of the West African Monsoon (WAM) in the south and of the subtropical North Atlantic in the west. Associated lifting generates an elevated dust layer, the "Saharan Air Layer" (SAL), which, on seasonal average, reaches a maximum of about 4 km above sea level and, not uncommonly, can reach to altitudes of 6 km [*Karyampudi et al.*, 1999; *Schepanski et al.*, 2009; *Knippertz and Todd*, 2012]. Satellite data and multimodel intercomparison confirm this annual cycle of dust centroid height over North Africa and the eastern Atlantic Ocean [*Kim et al.*, 2014].

Most studies on the transatlantic dust transport so far analyzed either short episodes, measurements at single stations, or data from satellite retrievals. For example, *Pierangelo et al.* [2004] investigated mineral dust optical depth and altitude with satellite-based measurements of the Advanced Infrared Radiation Sounder (AIRS) for the period from April to September 2003. For the region of Cape Verde, they found an increasing height of the dust layer from spring to summer. *Schepanski et al.* [2009] used simulations with a regional model system that includes multiscale chemical aerosol transport for case studies in different seasons in 2006/2007. *Engelstaedter et al.* [2009] analyzed dust concentration measurements at Barbados between 1980 and 1992 and calculated back trajectories from Barbados, driven by European Centre for Medium-Range Weather Forecasts (ECMWF) reanalysis wind fields, without considering the dust concentration and deposition during the transport. They found the transport of dust from the northwestern African coast to Barbados to take 6 to 7 days. *Yu et al.* [2015] summarized estimates of dust deposition into the Amazon Basin from different studies ranging from 13 to 50 Tg yr^{-1}. Their own results, based on 7 year 3-D satellite retrievals of Cloud-Aerosol Lidar with Orthogonal Polarization (CALIOP) data show strong interannual variations between 8 and 48 Tg yr^{-1} with an average of 28 Tg yr^{-1}. They also point out the difficulties in comparing estimates from different studies because of different geographical definitions of the Amazon Basin, different years investigated, and methodological differences.

In contrast, this study uses data from a 5 year time slice simulation with the global chemistry climate model (GCCM) fifth generation ECMWF-Hamburg-model (ECHAM5)/Modular Earth Submodel System (MESSy) Atmospheric Chemistry (EMAC, see section 2.1). To the best of our knowledge, this is the first study employing temporally high resolved, four-dimensional output of a multiyear GCCM simulation to analyze the mineral dust cycle. This data set provides an ideal, long-term basis for investigating the above mentioned issues of the transatlantic dust transport. A novel combination of Eulerian and Lagrangian analyses is employed to address the various aspects of dust transport, benefiting thereby from the complementary characteristics of the two methodologies. The foci of our analysis are on transport pathways, transport duration, the localization of the main source regions in North Africa, and the seasonality of these characteristics.

Specifying the dust-source regions constitutes an important theme in the current research on transatlantic dust transport. *Trapp et al.* [2010] analyzed the elemental composition of dust samples collected at Barbados and Miami in the NH summers of 2003 and 2004, without reaching clear conclusions about the source regions of the measured dust. Some studies, e.g., by *Koren et al.* [2006] and *Tegen et al.* [2006], assigned a huge part of the dust reaching the Amazon Basin during NH winter to emissions from the Bodélé Depression, which is plausible since, overall, the Bodélé Depression is known to be the most active Saharan dust-source region in NH winter [*Washington et al.*, 2009; *Evan et al.*, 2015]; and *Schepanski et al.* [2009] found the conditions for long-range transport of dust from the Bodélé Depression to South America to be best during that season. The Bodélé Depression is also the major dust-emitting spot in the simulation used in this study (T85TG in *Gläser et al.* [2012]). However, *Scheuvens et al.* [2013] found important source regions for transatlantic dust transport in the central and western parts of the Sahara. Clearly, a detailed and direct investigation of the linkage between African emission regions and transport to the Americas is currently lacking.

This paper continues with a description of the data set and methodologies used (section 2), followed by an overview on the episodic character of the mineral dust cycle in section 3. The three-dimensional structure of the transatlantic transport is presented in section 4. It aims at comparing Eulerian and Lagrangian results and verifying the simulation with satellite observations. Section 5 highlights the advantages of the Lagrangian method in yielding typical transport durations. Section 6 contains the quantitative source region mapping of

21698996, 2015, 21, Downloaded from https://agupubs.onlinelibrary.wiley.com/doi/10.1002/2015JD023792 by Cochrane Czech Republic, Wiley Online Library on [01/05/2024]. See the Terms and Conditions (https://onlinelibrary.wiley.com/terms-and-conditions) on Wiley Online Library for rules of use; OA articles are governed by the applicable Creative Commons License

21698996, 2015, 21, Downloaded from https://agupubs.onlinelibrary.wiley.com/doi/10.1002/2015JD023792 by Cochrane Czech Republic, Wiley Online Library on [01/05/2024]. See the Terms and Conditions (https://onlinelibrary.wiley.com/terms-and-conditions) on Wiley Online Library for rules of use; OA articles are governed by the applicable Creative Commons License

dust that reaches the Americas, and the conclusions are presented in section 7. Technical details about the Lagrangian calculations are provided in the Appendix.

2. Model, Data, and Methods

2.1. EMAC Simulation

The EMAC model system couples the fifth generation European Centre Hamburg GCM (ECHAM5) [*Roeckner et al.*, 2006] to the Modular Earth Submodel System (MESSy) [*Jöckel et al.*, 2005, 2010]. With this global atmosphere-chemistry model, free-running 5 year time slice simulations, driven by initial and boundary conditions for the year 2000, are performed. Free-running means that there is no nudging toward the true atmospheric circulation of the year 2000 in the model. Each year rather represents one possible realization with sea surface temperatures and solar forcing valid for this particular year, which has been chosen because *Huneeus et al.* [2011] showed that year 2000 conditions, e.g., of observed surface dust concentrations at Barbados and Miami or the Aerosol Robotic Network (AERONET) coarse mode aerosol optical depth, are comparable with the average from 1996 to 2006. Thirty-one model layers, mainly located in the troposphere, with the top of the atmosphere at 10 hPa are employed. Four spectral truncations (T42, T63, T85, and T106), each with two different dust emission schemes [*Tegen et al.*, 2002; *Balkanski et al.*, 2004] were tested, and the entire mineral dust cycle of these simulations was evaluated in *Gläser et al.* [2012], who also provide more details about EMAC and the model setup. *Gläser et al.* [2012] compared dust deposition fluxes and concentrations with long-term measurements at more than 100 sites. Global and regional, and annual and seasonal comparisons with other model studies, and Moderate Resolution Imaging Spectroradiometer (MODIS) satellite data were also performed. Furthermore, simulated case studies were compared with Saharan Mineral Dust Experiment (SAMUM) measurements, Meteosat Second Generation satellite data, and the Barcelona Supercomputing Center/Dust Regional Atmospheric Model (BSC/DREAM). All these comparisons revealed that the model is able to represent the mineral dust cycle for year 2000 conditions in a realistic way [*Gläser et al.*, 2012]. Best results for the characteristics of the dust cycle were obtained with the spectral resolution of T85 (about 155 km horizontal grid spacing) and the dust emission scheme by *Tegen et al.* [2002]. Therefore, all analyses of the transatlantic dust transport presented here are based on the 5-hourly output of this simulation, referred to as T85TG in *Gläser et al.* [2012]. For the details of the model evaluation, we refer to *Gläser et al.* [2012]. New comparisons of this simulation with CALIOP satellite data are presented in section 4.

2.2. Eulerian Diagnostic

In this study, a combination of Eulerian and Lagrangian methods reveals detailed characteristics of the dust transport from North Africa to the Americas. Eulerian analyses (i.e., diagnostics based upon the 5-hourly grid point values) are used to quantify the absolute emission, deposition, and zonal fluxes of dust as simulated by the model. The horizontal and vertical structure of the main transport pathways and their seasonality are also described with Eulerian model output. Other characteristics as the transport time can be more accurately and straightforwardly investigated from the Lagrangian perspective (i.e., with the aid of trajectory calculations). However, to guarantee consistency of Eulerian and Lagrangian evaluations, most analyses in this study are performed with both methods and then compared to each other. To prevent confusion, all quantities have an index EUL or LAG if calculated from Eulerian and Lagrangian data, respectively.

For the upcoming analyses, 5 year time series of various variables in different regions (depicted in Figure 1a) are calculated, namely:

1. The surface dust emission flux, EMI_{EUL} (μg m^{-2} s^{-1}), averaged over entire North Africa and the Arabian Peninsula (brown area in Figure 1a) is shown in Figure 2a. For analyses in section 6.2, EMI_{EUL} is separately calculated for the western part of the Sahara (orange box in Figure 1a) and for the Bodélé Depression in Chad (yellow box in Figure 1a; both not shown in Figure 2a).
2. The westward dust transport TRA, i.e., dust concentration times zonal wind velocity (westward is positive here), is calculated across each tenth meridian from 10°W to 60°W and shown at 30°W ($TRA_{EUL}^{30°W}$) in Figure 2b. TRA is averaged from 20°S to 40°N and from the surface to 10 hPa for time series analyses.
3. The deposition flux DEP_{EUL} (μg m^{-2} s^{-1}) of dust in Caribbean (CAR) and Amazon Basin (AMA), which corresponds to the actual Eulerian surface dust deposition fluxes in these regions, is depicted in Figure 2c.

The distribution of all three variables are strongly positively skewed. The Yule-Kendall skewness statistic γ_{YK} as defined in *Wilks* [1995] amounts to $\gamma_{YK}(TRA_{EUL}^{30°W}) = +0.37$, $\gamma_{YK}(DEP_{EUL}$ in AMA$) = +0.50$ and $\gamma_{YK}(DEP_{EUL}$ in CAR$) = +0.61$. To make the data more normal and less dependent on outliers for statistical

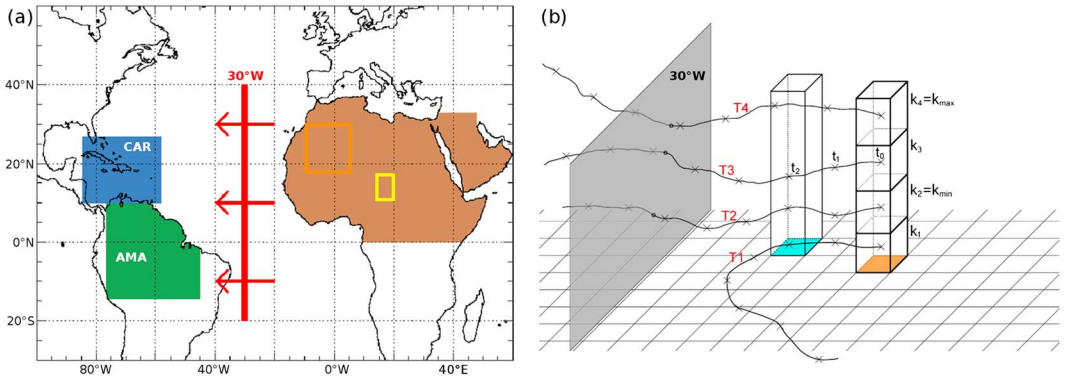

Figure 1. (a) The different regions of interest of this study: North Africa and the Arabian Peninsula (brown), the western part of the Sahara (orange box), the Bodélé Depression in Chad (yellow box), and the Caribbean (CAR, blue) and Amazon Basin (AMA, green). Trajectories must cross the 30°W meridian between 20°S and 40°N (bold red line) to be considered as potential Atlantic dust transport trajectories in this study. (b) A schematic to illustrate and explain the setup of Lagrangian calculations (see text in section 2.3 and the Appendix for details).

analyses, all time series undergo the Box-Cox-Transformation $y = ln(x)$ [*Wilks*, 1995] reducing the skewness to $\gamma_{YK}(\mathrm{TRA}_{\mathrm{EUL}}^{30^\circ\mathrm{W}}) = -0.03$, $\gamma_{YK}(\mathrm{DEP}_{\mathrm{EUL}}$ in AMA$) = +0.05$, and , $\gamma_{YK}(\mathrm{DEP}_{\mathrm{EUL}}$ in CAR$) = -0.08$. Time-lagged correlations (Pearson product moment correlation, *Wilks* [1995]) of the normalized time series provide information about the transport time. For instance, the time shift yielding the maximum correlation coefficient between the time series of $\mathrm{TRA}_{EUL}^{30^\circ\mathrm{W}}$ and $\mathrm{DEP}_{\mathrm{EUL}}$ in CAR serves as an Eulerian estimate of the mean duration of dust transport from 30°W to the dust deposition in the Caribbean. For determining the lag with the maximum correlation, the time lag is varied in 5 h steps from 0 to 200 h (section 5.2).

2.3. Lagrangian Diagnostic

Air parcel trajectories, calculated with wind fields from the EMAC simulation, establish pathways from a dust emission region across the North Atlantic to dust deposition events. Therefore, they are, in principle, ideally suited for directly quantifying the transport time and the dust emission region associated with deposition in the Americas. For this reason, we also use a Lagrangian approach in this study employing the Lagrangian

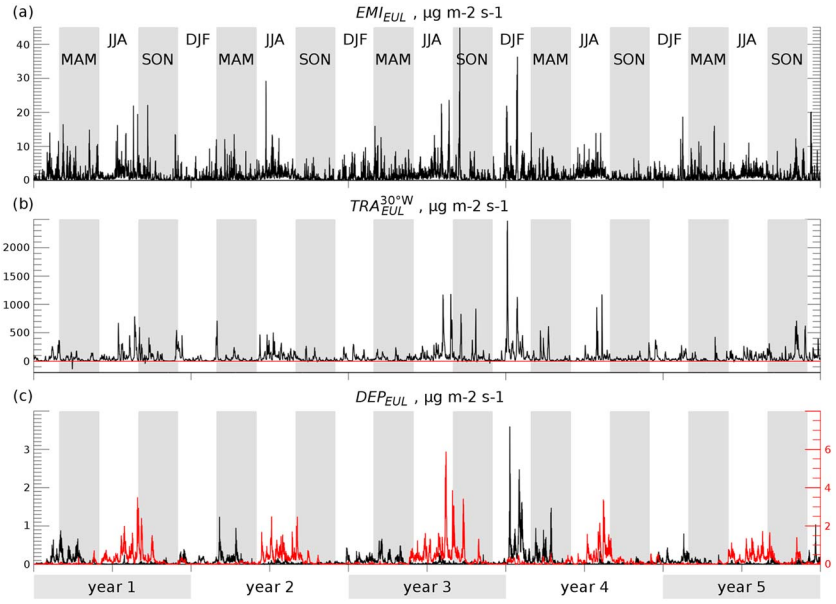

Figure 2. Five-year time series of (a) $\mathrm{EMI}_{\mathrm{EUL}}$, (b) $\mathrm{TRA}_{\mathrm{EUL}}^{30^\circ\mathrm{W}}$, and (c) $\mathrm{DEP}_{\mathrm{EUL}}$ as described in section 2.2. Figure 2c shows data for the Amazon Basin (black, left ordinate) and the Caribbean (red, right ordinate. Note that the ordinates differ by a factor of 2.). The Amazon Basin is restricted to the green part in Figure 1a located south of the equator to obtain a clearer seasonal variation. Labels for year 1 to year 5 on the abscissa denote the respective year of the time slice simulation.

21698996, 2015, 21, Downloaded from https://agupubs.onlinelibrary.wiley.com/doi/10.1002/2015JD023792 by Cochrane Czech Republic, Wiley Online Library on [01/05/2024]. See the Terms and Conditions (https://onlinelibrary.wiley.com/terms-and-conditions) on Wiley Online Library for rules of use; OA articles are governed by the applicable Creative Commons License

21698996, 2015, 21, Downloaded from https://agupubs.onlinelibrary.wiley.com/doi/10.1002/2015JD023792 by Cochrane Czech Republic, Wiley Online Library on [01/05/2024]. See the Terms and Conditions (https://onlinelibrary.wiley.com/terms-and-conditions) on Wiley Online Library for rules of use; OA articles are governed by the applicable Creative Commons License

Table 1. Number of Trajectories Initialized and Reaching CAR and AMA[a]

		CAR				AMA			
	Initialized #	DEP_{EUL}	DEP_{LAG}	#	%	DEP_{EUL}	DEP_{LAG}	#	%
DJF	152,357	1.8	0.7	21,556	(14)	8.9	4.9	100,387	(66)
MAM	102,534	2.1	0.9	20,437	(20)	9.1	2.8	54,355	(53)
JJA	257,403	21.1	10.0	140,809	(55)	8.5	2.4	64,973	(25)
SON	143,331	9.3	2.2	47,009	(33)	3.8	1.3	47,092	(33)
$\sum$	655,625	34.3	13.8	229,847	(35)	30.3	11.4	266,807	(41)

[a]The share of trajectories reaching CAR and AMA in each season is listed in parentheses. The values in the DEP_{EUL} and DEP_{LAG} columns give the amount of dust in Tg per season that is deposited in the respective region, depending on the method. Annual values are listed in the last line.

Analysis Tool (LAGRANTO) [*Wernli and Davies*, 1997]. A comprehensive set of 15 day forward trajectories is calculated, starting from North Africa and the Arabian Peninsula at each simulation output time step and each grid box within the planetary boundary layer if the local dust emission flux is greater than zero. For the transatlantic dust transport, the relevant trajectories are selected with the simple criterion that they cross 30°W between 20°S and 40°N. This criterion is fulfilled for the exemplary, schematic trajectories T_2, T_3, and T_4 in Figure 1b but not for T_1. In total, more than 650,000 trajectories crossing 30°W are the basis of the Lagrangian analyses in this study (Table 1).

Tracing the dust mixing ratio along the trajectories provides additional information about where air masses pick up dust (due to turbulent mixing in the boundary layer or sedimentation from above) or lose dust (due to sedimentation or wet scavenging). The potential of such a Lagrangian approach has already been shown, e.g., by *Sodemann et al.* [2006] or by *Gläser et al.* [2012] for case studies of individual dust transport events to Central Europe. However, it turns out that a systematic quantitative analysis of the dust cycle in multiannual EMAC simulations using trajectories, which is fully consistent with the Eulerian diagnostics (see above), is challenging, mainly for the following reason. Information about accumulated surface dust emission at a specific grid point is available every 5 h. Within this time period, the freshly emitted dust is likely to be vertically mixed in the turbulent boundary layer. However, the degree of this vertical mixing is unknown. This has two important consequences for the setup of the trajectory calculations:

1. For dust emission at a certain grid point, forward trajectories must be started at all vertical levels in the boundary layer (see Figure 1b), since they all might be "affected" by the freshly emitted dust. Calculating forward trajectories from the lowest model level only (which is closest to the actual emission with an averaged layer height of about 5 hPa ≈ 40 m above the surface), would most certainly underestimate dust transport because of the typically weaker winds near the surface.
2. The initial dust mixing ratio at the starting points of these trajectories is not entirely due to surface emission during the previous 5 h, but of course also influenced by the previous dust load in the boundary layer. Therefore, a weighting factor has to be introduced, which is based on estimates of the contribution of the surface dust emission to the initial dust mixing ratio. The effect of this procedure, which is explained in detail in section A1, is that for the subsequent Lagrangian analyses, trajectories starting from very dusty grid points where current emissions are weak have a low weight, whereas those from grid points where current emissions are strong are weighted more prominently.

Figure 3 provides an illustrative example of the Lagrangian approach. For an arbitrarily selected peak in $TRA_{EUL}^{30°W}$ in January of the third year of the simulation, the dust mixing ratio along the selected trajectories, which are associated with dust emission over North Africa and dust transport across 30°W, is shown in Figure 3. In this example, most of the trajectories originate from the western part of the Sahara and carry a huge amount of dust, in parts more than 500 μg kg^{-1} (i.e., μg dust per kg air) During the transatlantic transport within the trade wind layer, dust particles are removed by sedimentation or wet deposition; and most of the trajectories reach South America with dust mixing ratios of less than 20 μg kg^{-1}. Over the Amazon, the remaining dust is scavenged and the trajectories move into the South Atlantic region with virtually no dust. Very few trajectories cross 30°W, then rise, and travel eastward as far as India.

For the comparison with the Eulerian approach, two quantities that can be easily quantified with grid point values, i.e., the seasonally integrated net dust emission field ΔDU and the seasonally integrated net zonal dust

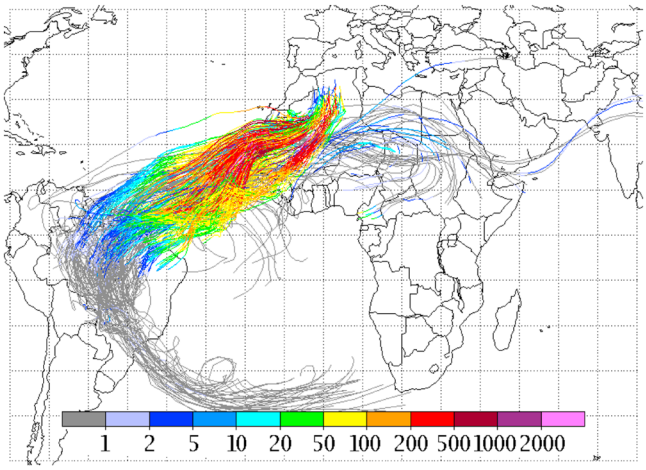

Figure 3. Example of 15 day forward trajectories associated with dust emission over North Africa and cross-Atlantic transport. All trajectories are initialized over North Africa at one EMAC output time step, and they all travel across 30°W during the next 15 days. The color code shows the dust mixing ratio along the trajectories in μg kg^{-1}.

flux across a certain meridian, TRA, are also estimated based upon the trajectory data, as further explained in the Appendices A2 and A3. The grid point quantity ΔDU_{LAG} represents the vertically integrated net dust gain along transatlantic trajectories crossing the considered grid box. Therefore, ΔDU_{LAG} tells us where trajectories on average gain and lose their dust and therefore provides information about main source and deposition regions. Furthermore, it allows connecting a grid box with negative values of ΔDU_{LAG}, i.e., a place where dust is deposited, with the origin of this dust, which is the starting point of the respective trajectory (see section 6). With this type of Lagrangian estimates, an element of uncertainty is that the dust lost by a particular trajectory might not be deposited at this place but transported farther by an air parcel located below.

3. The Episodic Nature and Variability of Dust Emission, Transport, and Deposition

Images of satellite measured aerosol optical depth or simulated dust properties, temporally averaged over months, seasons, or even longer periods, as depicted in, e.g., *Peyridieu et al.* [2010], *Miller et al.* [2006], or in Figure 4 of this study, suggest a continuous transport of dust from North Africa across the Atlantic. However, each component of the atmospheric dust cycle underlies diurnal [*Heinold et al.*, 2013; *Fiedler et al.*, 2013], intraseasonal [*Engelstaedter et al.*, 2006], annual [*Engelstaedter and Washington*, 2007; *Prospero et al.*, 2014], and interannual variations [*Prospero and Lamb*, 2003; *Mahowald et al.*, 2003; *Chiapello et al.*, 2005; *Doherty et al.*, 2008, 2014], and it is important to realize that this climatological dust plume is the result of many individual, more or less separated events of Saharan dust outbreaks, illustrated by single peaks in the time series of dust transport TRA_{EUL} across 30°W (Figure 2b).

These strong fluctuations occur due to a combination of different factors that influence the dust transport. First, dust emission itself depends on the meteorological conditions in the dust-source regions and is highly variable, as shown in Figure 2a. Peak values exceed the long-term average by more than an order of magnitude. High wind speed, capable of mobilizing a large amount of dust particles, is caused by different processes on different spatial scales, including cyclones, Harmattan surges, African easterly waves, low-level jets, cold pools, or dust devils [*Knippertz and Todd*, 2012].

A second factor is the transport direction, which is subject to the large-scale circulation. Saharan dust is transported not only toward the North Atlantic but also across the whole NH to Europe, North America, Asia, and the Pacific Ocean [*McKendry et al.*, 2007; *Hsu et al.*, 2012; *Varga et al.*, 2013]. Therefore, strong dust emission events need to coincide with easterly winds to produce a peak in the TRA_{EUL} time series. As can be seen in Figures 2a and 2b, some peaks in EMI_{EUL} also lead to peaks in TRA_{EUL}, but the signal is clearly strongly modulated by transport and dust deposition before reaching 30°W. As for EMI_{EUL}, also for TRA_{EUL} the amplitude of individual peaks can exceed the mean value by more than an order of magnitude.

The transient nature of the atmospheric dust cycle is also very obvious when looking at the time series of dust deposition in the regions AMA and CAR (Figure 2c). Many peaks in TRA_{EUL} translate into clear peaks in

21698996, 2015, 21, Downloaded from https://agupubs.onlinelibrary.wiley.com/doi/10.1002/2015JD023792 by Cochrane Czech Republic, Wiley Online Library on [01/05/2024]. See the Terms and Conditions (https://onlinelibrary.wiley.com/terms-and-conditions) on Wiley Online Library for rules of use; OA articles are governed by the applicable Creative Commons License

deposition, again with additional modulation due to transport and the variable occurrence of precipitation in the target regions. Very striking in this figure is the very pronounced seasonal cycle in the preference for deposition in one of the two regions. Deposition in AMA occurs mainly in December-January-February (DJF) and March-April-May (MAM), whereas deposition in CAR peaks in June-July-August (JJA) and September-October-November (SON). Within the preferred seasons for deposition in AMA or CAR there is still large day-to-day variability, resulting from the variability in transport and wet deposition.

Climatic variations in West Africa, as for instance the variability of Sahelian rainfall [*Nicholson et al.*, 1998], which influence dust emissions and the atmospheric dust load on decadal and longer time scales [*Mukhopadhyay and Kreycik*, 2008] are not captured by our simulations that are driven by external fields valid for the year 2000. The 5 year time slice simulation provides a range of realizations and allows to estimate the uncertainty of the global dust cycle due to internal atmospheric variability. For instance, the North African dust emission flux varies between 800 and more than 1000 Mt yr^{-1}. Because these fluctuations do not account for uncertainties in variability of the forcing fields, they clearly only capture parts of the dust cycle's interannual variability. Also long-term climate variability of the West African climate and the mineral dust cycle [*Nicholson*, 2009; *Cowie et al.*, 2013], and its variations related to El Niño – Southern Oscillation and the North Atlantic Oscillation [*DeFlorio et al.*, 2015] are not represented in our results.

4. Transport Pathways

The Eulerian perspective is ideally suited to provide the mean characteristics of dust emission, deposition, and fluxes as simulated in the model. Therefore, the following analyses start with the description of Eulerian results. The then following comparison with the Lagrangian approach validates whether the calculated trajectories are representative of the Eulerian data. The averaged net dust emission flux, i.e., the difference field between the dust emission and deposition fluxes (ΔDU), serves to obtain an overview on the long-term source and deposition regions (section 4.1). The vertical structure of the dust transport is described using height-latitude cross sections of the westward dust transport across different meridians in section 4.2. The discussion and comparison with observations follows in section 4.3.

4.1. Horizontal Structure

Net dust emission fluxes are shown in Figure 4 for the seasons DJF and JJA. The definitions of ΔDU_{EUL} and ΔDU_{LAG} are given in the Appendices A1 and A2, respectively. Reddish colors show the net source regions, and bluish colors the net deposition regions of mineral dust according to our simulation.

4.1.1. Eulerian Approach

The Sahara is clearly not a uniform dust-source region. Distinct emission maxima are found over Mauritania and Mali, in particular in JJA (Figures 4a and 4c). Clear maxima of ΔDU_{EUL} also occur in the Bodélé Depression, in particular in DJF (Figure 4a) when the dust is mainly transported to and deposited in the south and southwest. In JJA, the ITCZ is positioned north of the Bodélé Depression, and dust emitted there is in part transported northward to the Tibesti mountains, causing the strong negative values near 20°N/15°E just north of the emission hot spot (Figure 4c). Another deposition maximum with negative values of ΔDU_{EUL} occurs near 25°N/5°E, i.e., in the Hoggar mountains where the soil conditions inhibit dust emission and dust from the surrounding source regions is deposited. Overall, the strongest negative fluxes are downstream of and fairly close to the prominent dust emission regions, showing the fast settling of large particles shortly after the emission. In JJA, a band with very strong deposition appears in the west African monsoon region along 10°N. Also visible are patterns of dust emission and deposition in Central Asia and South Africa, which are, however, not considered further in this study since its focus is on North Africa, the adjacent Atlantic, and the Americas. Over the Atlantic, the seasonal variation is clearly visible with the major dust transport to and deposition in a broad band toward South America in DJF (and MAM, not shown) and the more zonal transport to the Caribbean in JJA (and SON, not shown).

We like to point to the local deposition maximum over the Alpine region in JJA (Figure 4c), which agrees with earlier case studies, [e.g., *Sodemann et al.*, 2006; *Gläser et al.*, 2012] describing northward Saharan dust transport events to Central Europe.

4.1.2. Comparison With the Lagrangian Approach

Many Eulerian features of the net dust emission flux are well represented by the Lagrangian approach, both in terms of the horizontal distribution and the absolute values (compare Figures 4a with 4b, and 4c with 4d). The seasonal differences of the transatlantic dust transport are also well reproduced by the Lagrangian method.

21698996, 2015, 21, Downloaded from https://agupubs.onlinelibrary.wiley.com/doi/10.1002/2015JD023792 by Cochrane Czech Republic, Wiley Online Library on [01/05/2024]. See the Terms and Conditions (https://onlinelibrary.wiley.com/terms-and-conditions) on Wiley Online Library for rules of use; OA articles are governed by the applicable Creative Commons License

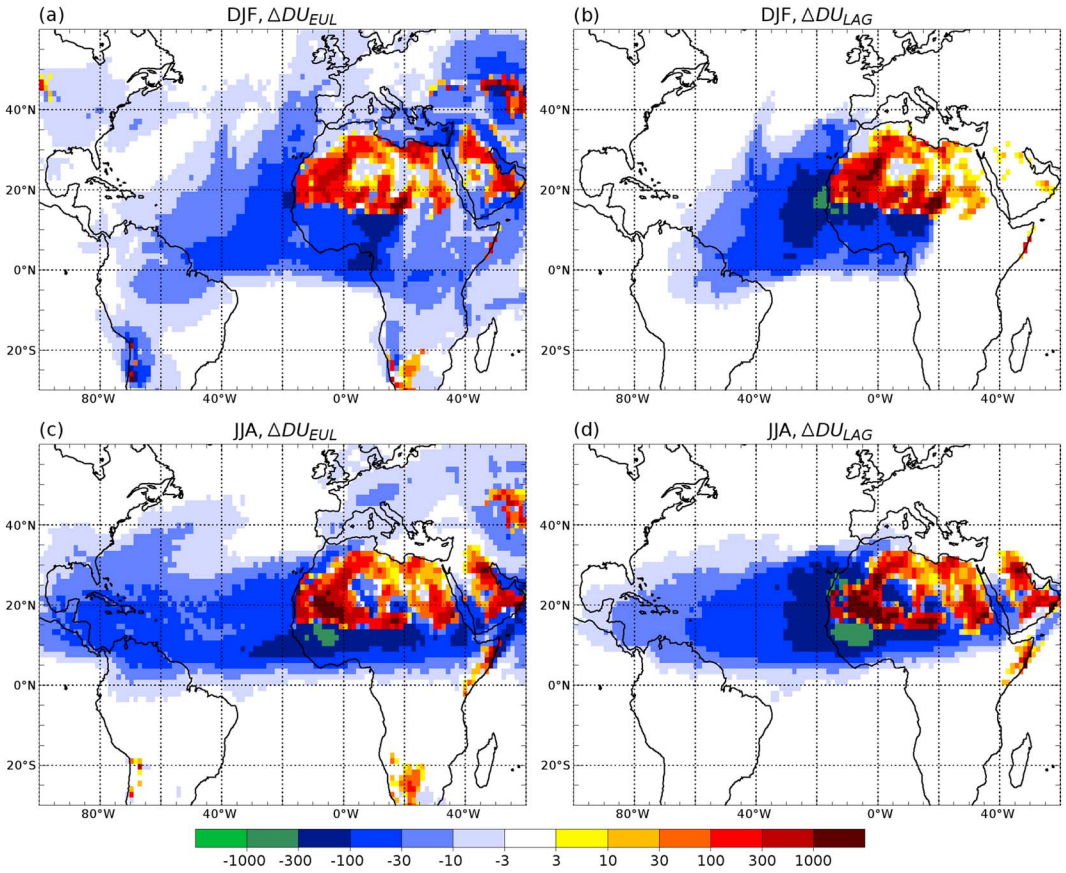

Figure 4. Net dust emission fluxes (left column) ΔDU_{EUL} and (right column) ΔDU_{LAG} in kg ha^{-1} per season for (top row) DJF and (bottom row) JJA. Positive values denote net dust emission, and negative values net dust deposition.

Furthermore, smaller-scale features are comparable, like the deposition maxima in the central Sahara in JJA and the emission peaks in Mali/Mauritania in the same season. The distribution and absolute values of the dust emission in the Bodélé Depression and the deposition downstream also agree very well between the two approaches.

In both seasons ΔDU_{LAG} slightly overestimates the dust deposition southwest of the Mali/Mauritania emission region compared to ΔDU_{EUL}. This indicates the possibility that dust, removed from the trajectories in this region by sedimentation, is transported further by air masses below the considered trajectories. This process is not captured by our Lagrangian approach. Consequently, the deposition is higher in the Eulerian data in the remote regions of the Amazon and the Caribbean. The absence of any signal in ΔDU_{LAG} in Central Asia and South Africa is simply because no trajectories have been started in these areas. And the zero signal in Europe indicates that transport to Europe does typically not first cross the meridian at 30°W (recall that we only consider trajectories that cross this meridian).

In accordance with the Eulerian results, the number of initialized trajectories peaks in JJA (Table 1), when Saharan dust emission activity is maximum. Of all trajectories 35% reach the Caribbean, 82% of them in JJA and SON. The Amazon Basin is reached by 41%, of which almost 60% arrive there in DJF and MAM. The remaining quarter of the trajectories crosses 30°W but does not reach one of the target regions within 15 days after the initialization. Table 1 lists also the averaged amount of dust deposited in the Caribbean and the Amazon Basin. The Eulerian deposition amounts to 34.3 Tg yr^{-1} in the Caribbean and 30.3 Tg yr^{-1} in the Amazon Basin. Only about 40% of these values are represented by the trajectories (13.8 Tg yr^{-1} in CAR and 11.4 Tg yr^{-1} in AMA). During the main seasons of interest, i.e., JJA in CAR and DJF in AMA, the Lagrangian approach reproduces about half of the Eulerian fluxes. These important differences between the Eulerian and Lagrangian results arise from the completely different methodological approaches, as discussed above. The main missing part of the Lagrangian approach is that dust sedimenting out of the considered air parcels is "lost" for

21698996, 2015, 21, Downloaded from https://agupubs.onlinelibrary.wiley.com/doi/10.1002/2015JD023792 by Cochrane Czech Republic, Wiley Online Library on [01/05/2024]. See the Terms and Conditions (https://onlinelibrary.wiley.com/terms-and-conditions) on Wiley Online Library for rules of use; OA articles are governed by the applicable Creative Commons License

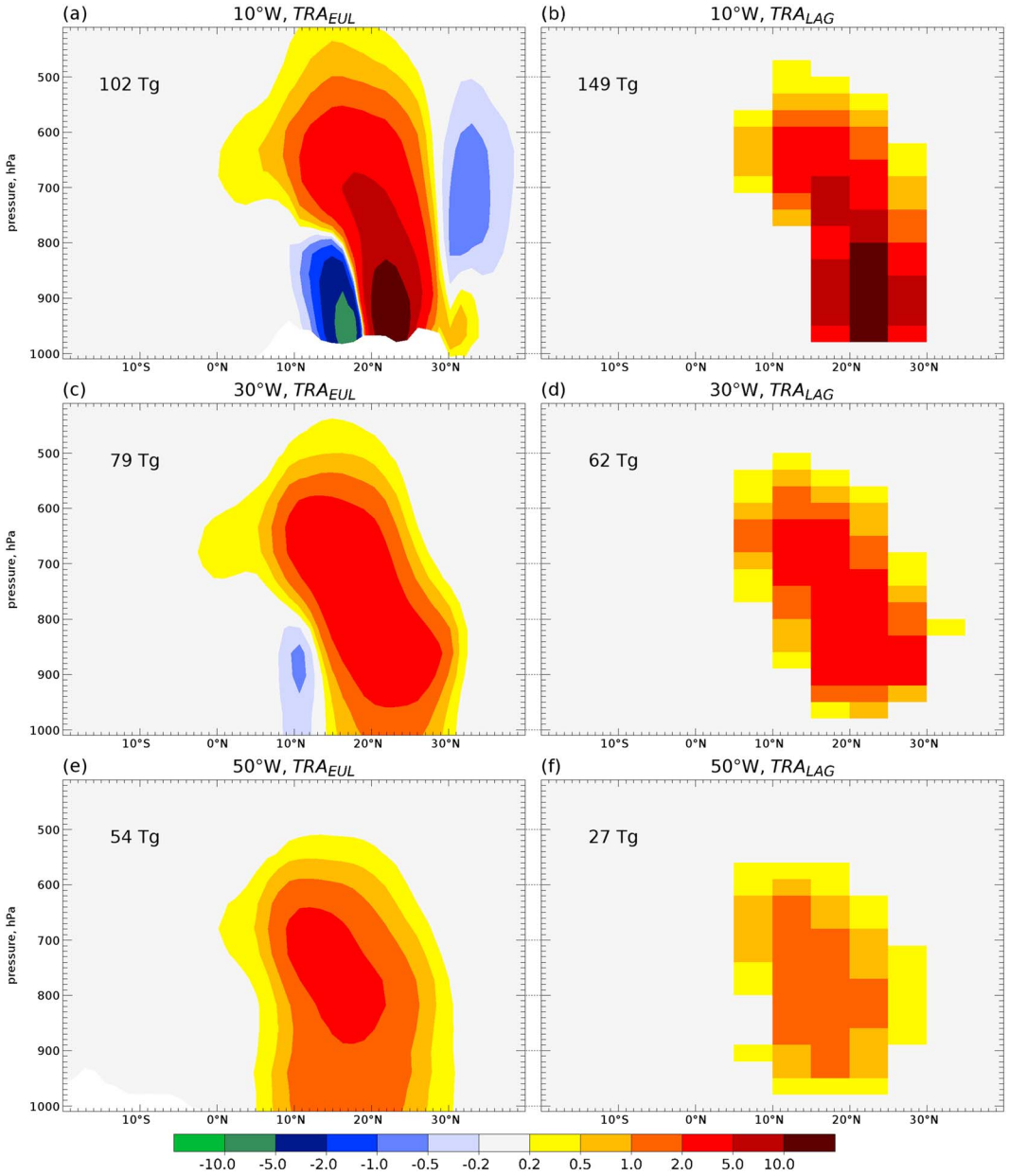

Figure 5. Meridional cross sections of the JJA westward dust transport (TRA in kg m^{-2} per month) across the meridians at (a, b) 10°W, (c, d) 30°W, and (e, f) 50°W. Figures 5a, 5c, and 5e show TRA_{EUL}, Figures 5b, 5d, and 5f show TRA_{LAG}, and the number in each panel denotes the integrated (from 20°S to 40°N and from the surface to 10 hPa) westward zonal dust flux (in Tg per season).

this approach, whereas it might be carried further by lower level air parcels, which are considered by the Eulerian but not the Lagrangian method. Nevertheless, the very good agreement of the spatial distribution of ΔDU_{EUL} and ΔDU_{LAG} in Figure 4 indicates that the trajectories have been reasonably well chosen, which is corroborated in the following sections.

4.2. Vertical Structure

Vertical cross sections from the surface to 400 hPa and from 20°S to 40°N of the monthly accumulated westward dust transport TRA across 10°W, 30°W, and 50°W are shown in Figure 5 during JJA, again for both the Eulerian (as defined in section 2.2; Figures 5a, 5c and 5e) and Lagrangian methods (as defined in section A3; Figures 5b, 5d, and 5f). For the three other seasons, the dust flux is only shown across 10°W in Figure 6. Positive and negative values show transport toward the west and east, respectively.

21698996, 2015, 21, Downloaded from https://agupubs.onlinelibrary.wiley.com/doi/10.1002/2015JD023792 by Cochrane Czech Republic, Wiley Online Library on [01/05/2024]. See the Terms and Conditions (https://onlinelibrary.wiley.com/terms-and-conditions) on Wiley Online Library for rules of use; OA articles are governed by the applicable Creative Commons License

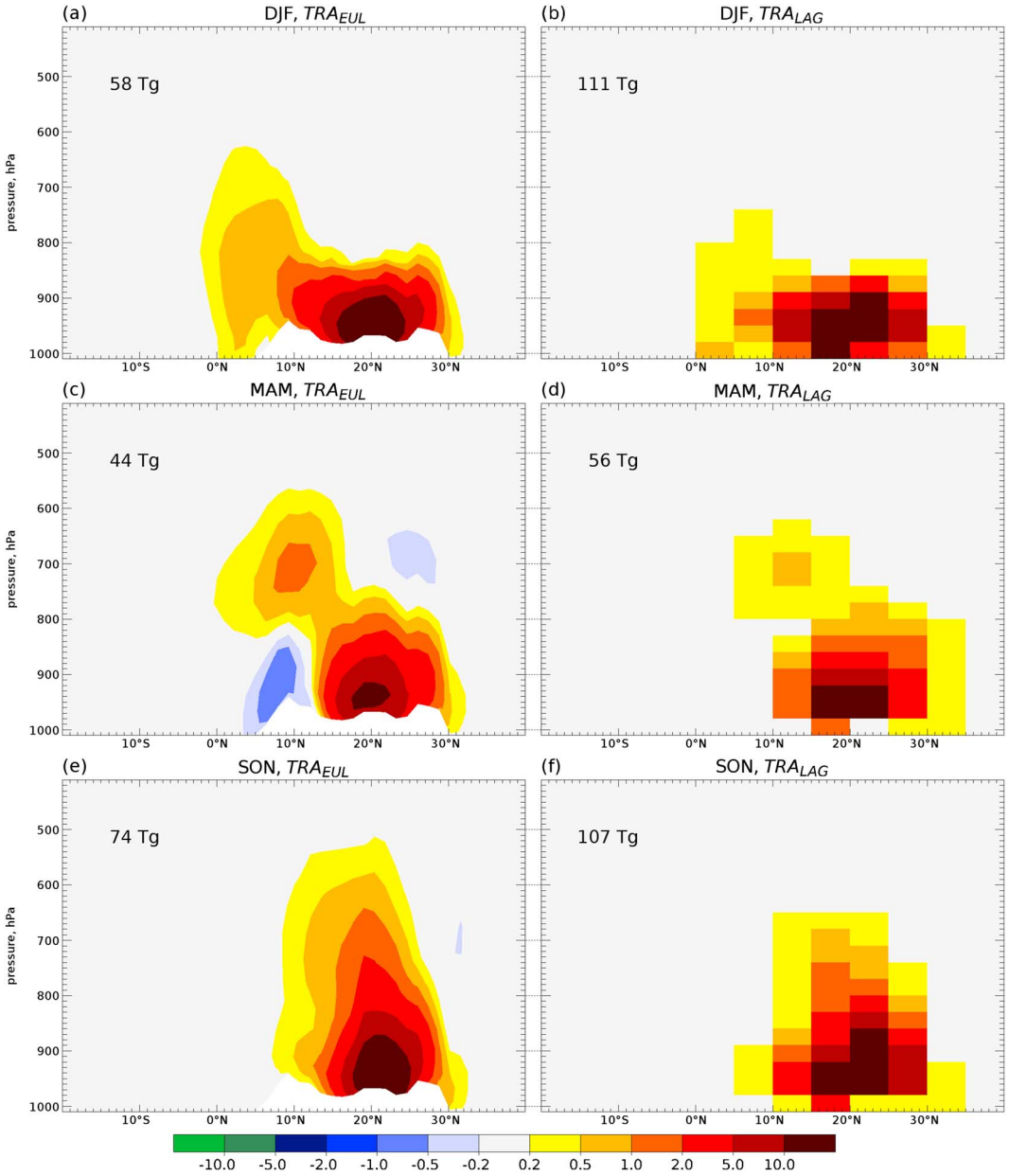

Figure 6. Meridional cross sections of the westward dust transport (TRA in kg m^{-2} per month) across the meridian at 10°W during (a, b) DJF, (c, d) MAM, and (e, f) SON. Figures 6a, 6c, and 6e show TRA_{EUL}, Figures 6b, 6d, and 6f show TRA_{LAG}, and the number in each panel denotes the integrated (from 20°S to 40°N and from the surface to 10 hPa) westward zonal dust flux (in Tg per season).

4.2.1. Eulerian Approach

In JJA, vertical mixing within the deep planetary boundary layer over the Sahara causes high dust concentrations up to 500 hPa and higher at 10°W (Figure 5a). The elevated SAL is advected westward above the trade wind inversion with maximum values between 600 and 900 hPa at 30°W (Figure 5c) and 50°W (Figure 5e). Advection over the cooler inflow of the WAM from southwest creates a two-layer structure at 10°W south of 20°N with westward dust export above and eastward dust transport below 800 hPa (Figure 5a). Rarely, the eastward flux dominates the integrated transport even across 30°W visible in negative values of $TRA_{EUL}^{30°W}$ in Figure 2b. In DJF, cyclonic storms and Harmattan surges cause high dust concentrations in the lowest 1.5 km over the Sahara [*Knippertz and Todd*, 2012]. Farther south, dust is mixed to higher levels within the ITCZ (Figure 6a), where it is washed out quickly. The transatlantic transport happens within the trade wind layer at levels below 850 hPa associated with a southward shift of the maximum from 16–20°N at 20°W to 9–12°N

21698996, 2015, 21, Downloaded from https://agupubs.onlinelibrary.wiley.com/doi/10.1002/2015JD023792 by Cochrane Czech Republic, Wiley Online Library on [01/05/2024]. See the Terms and Conditions (https://onlinelibrary.wiley.com/terms-and-conditions) on Wiley Online Library for rules of use; OA articles are governed by the applicable Creative Commons License

21698996, 2015, 21, Downloaded from https://agupubs.onlinelibrary.wiley.com/doi/10.1002/2015JD023792 by Cochrane Czech Republic, Wiley Online Library on [01/05/2024]. See the Terms and Conditions (https://onlinelibrary.wiley.com/terms-and-conditions) on Wiley Online Library for rules of use; OA articles are governed by the applicable Creative Commons License

at 60°W (not shown). MAM and SON show transient characteristics with high dust concentrations up to 600 hPa at 10°W (Figures 6c and 6e). In MAM, the evolution of the two-layer structure is already visible south of about 13°N.

4.2.2. Comparison With the Lagrangian Approach

The westward transport, vertically and latitudinally integrated (numbers are given in Figures 5 and 6), reveals some discrepancies between the two techniques. At 10°W, the Lagrangian fluxes are on average 1.5 times higher than the Eulerian ones. Farther west the ratio of Lagrangian to Eulerian results decreases, and TRA_{LAG} is only half of TRA_{EUL} at 50°W. This is consistent with the results shown and for the reasons discussed in section 4.1.2. Another cause for higher integrated values of TRA_{LAG} close to the source regions at 10°W is the criterion chosen for the trajectory selection. As trajectories are only initialized over North Africa, the eastward transport back to the continent is underestimated. For example, no trajectories representing the WAM are considered, which would travel eastward from the Atlantic Ocean toward the West African coast, gain dust in this region, travel farther east, and transport the dust back to the continent. This Lagrangian underrepresentation of the eastward dust flux between 10°N and 20°N and up to 800 hPa within the monsoon wind layer can be nicely seen at 10°W in JJA (Figures 5a and 5b). At 30°W and 50°W, TRA_{EUL} has large values between about 600 hPa and the surface (Figures 5c and 5e), while TRA_{LAG} is fairly low beneath 950 hPa (Figures 5d and 5f). The reason for this difference is that the settling of dust is visible in the Eulerian data, whereas there are only few dust-laden trajectories below 950 hPa. The overall distribution of the Eulerian and Lagrangian fluxes, however, agrees well at different longitudes and in all seasons with maxima at the same latitudinal and vertical positions. Also, some finer structures are represented by the trajectories, like two maxima at 10°W in MAM near 10°N/700 hPa and 20°N/950 hPa (Figures 6c and 6d).

4.3. Discussion

Main characteristics of the dust cycle in our simulation are consistent with observations and other simulations as shown by *Gläser et al.* [2012]. More comparisons with deposition data from *Knippertz and Stuut* [2014] (their Figure 8.3) reveal an underestimation of dust deposition in the model by a factor of 1.5 to 2 (not shown). Discrepancies diminish with greater distance to the main source regions in the Sahara. The reason for this is that particles with diameters greater 15.88 μm are neglected in the model as such large particles are thought to fall out rapidly [*Prospero*, 1999]. Close to the source regions, however, these large particles can dominate measurements [*O'Hara et al.*, 2006] and explain higher observed than simulated dust deposition fluxes. Recent measurements indicate that there is also a contribution of larger dust particles (>20 μm) to the long-range transport [*Stuut and Prins*, 2014] which implies that the maximum diameter for aerosols in numerical models should be increased in order to include those particles. This could further improve simulations of the mineral dust cycle. Moreover, the simulated spatial distributions of dust emission and, consequently, transport and deposition strongly depend on the employed dust emission scheme [*Gläser et al.*, 2012; *Evan et al.*, 2015], and uncertainties with regard to the emissions are not captured in our simulation.

In *Gläser et al.* [2012], the evaluation of the model was restricted to near-surface or vertically integrated properties. Here the vertical distribution is considered as well and compared with measurements of the CALIOP instrument on the Cloud-Aerosol Lidar and Infrared Pathfinder Satellite Observation (CALIPSO) satellite [*Hunt et al.*, 2009]. When comparing CALIOP with model data, one needs to consider that the satellite data are available since 2006 while our time slice simulation represents year 2000 conditions. This complicates direct and quantitative comparisons of the data because of the interannual variation of the dust cycle [e.g., *Chiapello and Moulin*, 2002; *Prospero and Lamb*, 2003]. The average dust layer top height is above 5 km near the West African coast decreasing by about 30m per 1° longitude toward the west in JJA [*Ben-Ami et al.*, 2009; *Liu et al.*, 2012]. This is in agreement with the simulated top height of westward transport above 500 hPa at 10°W in Figures 5a and 5b which decreases at 30°W and 50°W. *Adams et al.* [2012] investigated the vertical distribution of CALIOP dust ''frequency-of-occurrence data. A qualitative comparison of our Figures 5 and 6 with their vertical cross sections (Figure 3 in *Adams et al.* [2012]) reveals general agreement in all seasons. For instance, in JJA the main transport occurs in an elevated layer with the center of the core around 3.5 km above ground at all longitudes. During winter the vertical extent is reduced, and cross sections show a bimodal structure with increasing top height from North to South. The transient characteristics of MAM and SON are also visible in the CALIOP data.

Without information about the wind fields, satellite data alone do not allow for statements on the transport direction. Besides the dominating westward dust export from the Sahara, there is a strong signal of eastward dust transport south of 20°N in the lowest 2 km of the atmosphere during NH summer in Figure 5a which is also

described by *Schepanski et al.* [2009]. The structure of the vertical distribution is dominated by the large-scale flow over West Africa and matches the illustration by *Cuesta et al.* [2009] (cf. Figure 5a with their Figure 1): Dust is vertically mixed in the planetary boundary layer up to levels above 5 km over the Sahara. South of the intertropical discontinuity dusty air masses from the north and northwest are dynamically lifted above the southwesterly monsoon surge, forming the SAL [*Cuesta et al.*, 2009]. Sedimentation of dust particles from the SAL into the monsoon layer and further transport within this layer generate the eastward dust flux as visible in Figure 5a.

These qualitative comparisons cannot verify the dust amounts transported across the Atlantic in our simulation. The spatial distributions, however, look realistic and, in combination with the evaluation of deposition data in *Gläser et al.* [2012], it seems plausible that both Eulerian and Lagrangian data represent the dust cycle in a realistic way. Considering that the simulation and satellite data do not represent the same time period, it is even more promising that the data fit that well. It suggests that many characteristics of the simulated year 2000 dust cycle are representative for a longer time span as indicated by *Huneeus et al.* [2011].

5. Transport Time

The Lagrangian approach allows to straightforwardly determine the duration of the dust transport from North Africa to the Americas and is therefore presented first in this section. Complementary information about transport times is revealed by time-lagged correlations of Eulerian data, which are described in section 5.2 followed by the discussion of the outcome in section 5.3.

5.1. Lagrangian Approach

With the Lagrangian approach, mean transport times are calculated as the time the trajectories need to reach 30°W ($\bar{\tau}_{LAG}^{30°W}$, equation (1)), and the target areas CAR and AMA, respectively. To reduce the impact of trajectories that transport only a small amount of dust, the time τ_{LAG} that each trajectory T_x needs to reach 30°W ($\tau_{\mathrm{LAG}}^{30°W}(T_x)$) is weighted with the trajectory's dust mixing ratio at 30°W ($DU_{\mathrm{mix}}^{30°W}(T_x)$):

$$\bar{\tau}_{\mathrm{LAG}}^{30°W} = \frac{\sum_x \left[DU_{\mathrm{mix}}^{30°W}(T_x) \cdot \tau_{\mathrm{LAG}}^{30°W}(T_x) \right]}{\sum_x DU_{\mathrm{mix}}^{30°W}(T_x)} \quad (1)$$

The sum over the index x captures all trajectories in one season X for X = DJF, MAM, JJA, and SON. For the transport to AMA and CAR, the duration ($\bar{\tau}_{\mathrm{LAG}}^{\mathrm{AMA}}$ and $\bar{\tau}_{\mathrm{LAG}}^{\mathrm{CAR}}$) is calculated accordingly but weighted with the dust mixing ratio when reaching AMA, respectively CAR.

The duration of the transport from the source regions to 30°W shows quite a large seasonal variation. $\bar{\tau}_{\mathrm{LAG}}^{30°W}$ reaches a value of 111 h (= 4 days and 15 h) in DJF, 174 h (= 7 days and 6 h) in MAM, 159 h (= 6 days and 15 h) in JJA, and 139 h (= 5 days and 19 h) in SON.

The following analyses are focusing on the seasons when most trajectories reach the Americas, namely DJF for AMA and JJA for CAR. The average time, see Table 2, from the emission to AMA during DJF $\bar{\tau}_{\mathrm{LAG}}^{\mathrm{AMA}}$ is 224 h (= 9 days and 8 h), and for the transport from emission to CAR during JJA it takes $\bar{\tau}_{\mathrm{LAG}}^{\mathrm{CAR}}$ = 247 h (= 10 days and 7 h). The individual seasons in the 5 year period with the fastest and slowest transport (listed in parentheses in Table 2) can be interpreted as the range of uncertainty in our simulations. The difference of $\bar{\tau}_{\mathrm{LAG}}^{\mathrm{AMA}} - \bar{\tau}_{\mathrm{LAG}}^{30°W}$ and $\bar{\tau}_{\mathrm{LAG}}^{\mathrm{CAR}} - \bar{\tau}_{\mathrm{LAG}}^{30°W}$ in the respective season yields the time that it takes the dust to travel from 30°W to the target regions. It is calculated for later comparison with the Eulerian data in section 5.3 and amounts to 4 days and 17 h (DJF, AMA) and 3 days and 16 h (JJA, CAR), respectively. Thus, the transport from 30°W to CAR in JJA is 1 day faster than to AMA in DJF.

As the dust content of the trajectories varies considerably, the upper 1% and the lower 75% of all trajectories with respect to their dust load are analyzed in more detail. Percentiles are selected with regard to the trajectories' dust mixing ratios when reaching the respective area. The upper 1% of all trajectories in DJF and in JJA transport 21% of the dust reaching 30°W, while the lower 75% account for 15% in DJF and 11% in JJA (Table 2). These percentiles are selected to be representative for the most extreme events like dust outbreaks to the Atlantic Ocean and for a more or less background state of the dust transport, respectively. The transport times of these percentiles are calculated for each season of the 5 year simulation separately. In general, during extreme events the dust moves faster—depending on season and region by 17 to 34 h—than the average over all trajectories while the lower 75% are slower by 10 to 43 h. The variability between the five simulated years is largest for the extremes and much smaller for the background state indicating that the characteristics of large dust outbreaks vary strongly.

21698996, 2015, 21, Downloaded from https://agupubs.onlinelibrary.wiley.com/doi/10.1002/2015JD023792 by Cochrane Czech Republic, Wiley Online Library on [01/05/2024]. See the Terms and Conditions (https://onlinelibrary.wiley.com/terms-and-conditions) on Wiley Online Library for rules of use; OA articles are governed by the applicable Creative Commons License

Table 2. Five-Year Averages of Lagrangian Transport Times ($\bar{\tau}_{LAG}$ in Hours According to Equation (1)) of Dust From Its Emission to 30°W, to AMA in DJF, and to CAR in JJA, Respectively[a]

			Upper 1%		All Trajectories		Lower 75%		
			$\bar{\tau}_{LAG}$	Share of Dust	$\bar{\tau}_{LAG}$		$\bar{\tau}_{LAG}$		Share of Dust
DJF	to 30°W	85	(70–100)	21%	111	(101–131)	154	(146–171)	15%
	to AMA	204	(183–240)	20%	224	(215–241)	237	(233–240)	14%
JJA	to 30°W	125	(103–139)	21%	159	(149–166)	190	(184–196)	11%
	to CAR	230	(199–249)	15%	247	(236–255)	257	(252–266)	19%

[a]The ranges in parentheses list the fastest and slowest seasons during the 5 years. The contribution of the upper 1 and the lower 75 percentiles to the dust reaching the respective region is listed as "share of dust." See text in section 5.1 for further details.

These Lagrangian results represent the time that the dust needs to reach the target regions. Combining Eulerian methods (section 5.2) with these Lagrangian results allows estimating the overall duration from dust emission to its deposition, which is presented in section 5.3 together with the discussion of the results.

5.2. Eulerian Approach

The duration of the first stage of the transport from the source regions in Africa to 30°W cannot be derived from the Eulerian time series, because the Eulerian emission data yield no information about the source regions of the dust that actually reaches 30°W. Time-lagged correlations, calculated as described in section 2.2, of normalized time series of $TRA_{EUL}^{30°W}$ and DEP_{EUL} are shown in Figure 7. The time shift associated with the maximum correlation coefficient is considered to represent the duration from dust crossing 30°W to its deposition in AMA, respectively CAR. In individual seasons, the correlation reaches maximum values for a time lag Δt between 105 and 150 h (on average 129 h = 5 days and 9 h) in DJF in AMA, and between 105 and 140 h (on average 121 h = 5 days and 1 h) in JJA in CAR (Figure 7). The ranges of 45 h in DJF and 35 h in JJA that seem to indicate quite a strong variability of the transport, which due to the restriction of our data set to only 5 years, might be even underestimated.

5.3. Synthesis of Both Approaches and Discussion

From 30°W to AMA and CAR, the Lagrangian approach yields mean transport times that are shorter by 16 h (AMA) and by 33 h (CAR) than the Eulerian method. This discrepancy arises from conceptual differences: In the Lagrangian approach, the mean time for reaching the border of the target region is calculated and the further penetration into the regions is not considered. Thus, the differences of 16 and 33 h, respectively, are an estimate of the time between reaching AMA or CAR and the dust deposition within the region. These differences need to be added to $\bar{\tau}_{LAG}$ to obtain the overall duration from the dust emission in North African source regions to the deposition in AMA and CAR. In DJF, the dust needs on average $\bar{\tau}_{LAG}^{AMA}$ + 16 h = 240 h (= 10 days), from the emission to the deposition in AMA with variations in the 5 year simulation of less than ±10%. In JJA it takes almost 2 days longer until the dust gets deposited in CAR ($\bar{\tau}_{LAG}^{CAR}$ + 33 h = 280 h (= 11 days and 16 h)), and the interannual variation is even smaller (Table 2). It is noteworthy that here the combination of the two approaches is essential to obtain the best possible transport time estimate from emission to deposition.

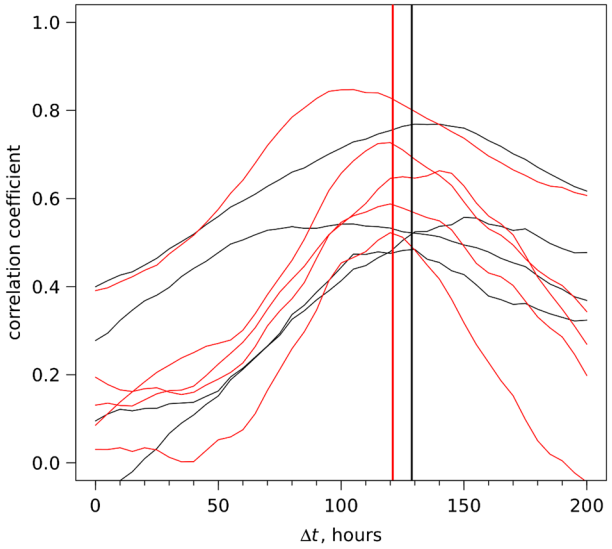

Figure 7. Time-lagged correlations of the normalized time series $TRA_{EUL}^{30°W}$ and DEP_{EUL}. Each black line shows one of the four DJF seasons for the transport from 30°W to AMA, red lines the five JJA seasons for the transport to CAR, respectively. Vertical lines mark the time shift of maximum correlation, averaged over the individual seasons.

21698996, 2015, 21, Downloaded from https://agupubs.onlinelibrary.wiley.com/doi/10.1002/2015JD023792 by Cochrane Czech Republic, Wiley Online Library on [01/05/2024]. See the Terms and Conditions (https://onlinelibrary.wiley.com/terms-and-conditions) on Wiley Online Library for rules of use; OA articles are governed by the applicable Creative Commons License

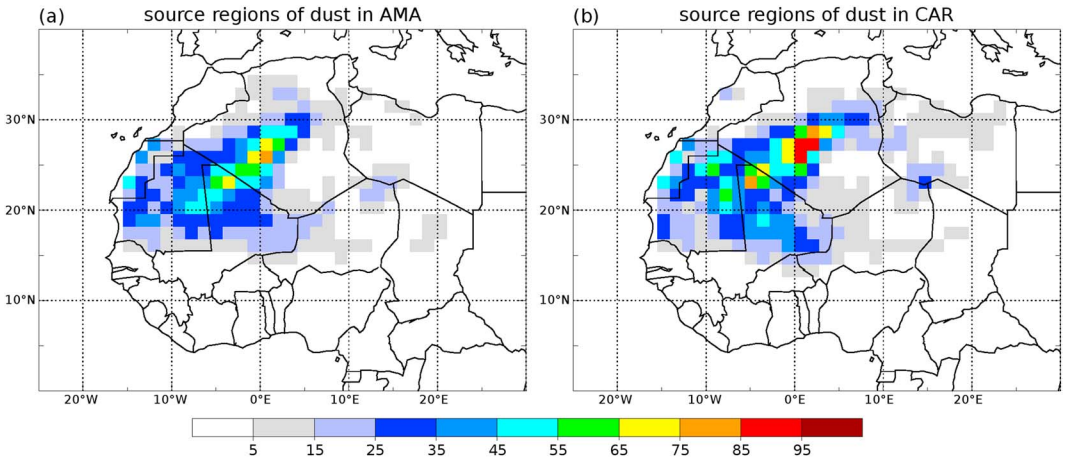

Figure 8. Source regions of dust reaching the Americas. The values correspond to the annual amount of emitted dust that is transported by the considered trajectories to (a) AMA and (b) CAR. The unit is kg ha^{-1} per year.

Engelstaedter et al. [2009] calculated backward trajectories from Barbados comparing days with high and low surface dust concentrations there. They considered days in June from 1980 to 1992 and received transport times between 6 and 7 days for the trajectories to reach the African coast, which is much shorter than the result for the transport to CAR in JJA found here. However, the authors did not account for the time it takes the dust to travel from the source region to the African coast. Our estimate of the Lagrangian mean transport time from 30°W to CAR in JJA amounts to $\bar{\tau}_{\mathrm{LAG}}^{\mathrm{CAR}} - \bar{\tau}_{\mathrm{LAG}}^{30^\circ\mathrm{W}} = 88$ h (Table 2). The distance from 30°W to CAR is about two thirds of the length from the African coast (around 15°W) to Barbados (59°W). Assuming similar transport velocities between the coast and 30°W and from there to CAR (eastern corner at 58°W), the Lagrangian method reveals a transport time of 88 h × 1.5 = 132 h (= 5 days and 12 h) for the distance from the African coast to Barbados, which is in very good agreement with the result of *Engelstaedter et al.* [2009] and another affirmation that the selected trajectories describe the transatlantic dust transport in a plausible way.

Another consistency with *Engelstaedter et al.* [2009] is that the selected dusty trajectories, i.e., the upper 1%, have the shortest transport time. The first part of the travel has the largest impact on the overall duration. During DJF, the mean difference of $\bar{\tau}_{\mathrm{LAG}}^{30^\circ\mathrm{W}}$ between the lower 75% and the upper 1% accounts to 154−85 = 69 h and to only 237−204 = 33 h for $\bar{\tau}_{\mathrm{LAG}}^{\mathrm{AMA}}$ (Table 2). The results for JJA are very similar with a difference of $\bar{\tau}_{\mathrm{LAG}}^{30^\circ\mathrm{W}}$ of 190−125 = 65 h and of $\bar{\tau}_{\mathrm{LAG}}^{\mathrm{CAR}}$ of 257−230 = 27 h. Confirming the importance of the first part of the transport, *Doherty et al.* [2014] found the flow over the Atlantic to have only secondary order effects on dust concentrations in the Caribbean, while conditions over West Africa, namely, the latitudinal position of the "West Africa Convergence Zone" (WACZ), dominate the dust export. Future work might investigate which of the dust emission processes described by *Knippertz and Todd* [2012] are favored to quickly reach the SAL where efficient long-range transport occurs, and if there is a relation to the position of the WACZ.

6. Source Regions

In this section, a particular strength of the Lagrangian method, namely, that dust is traced from its emission 15 days forward in time, is used to connect North African source regions with deposition in the Americas (section 6.1). Additional Eulerian analyses are presented in section 6.2, followed by the discussion (section 6.3).

6.1. Lagrangian Approach

The source regions of dust reaching the Americas are calculated in the following way: The loss of dust along the trajectories ΔDU_{LAG} is computed according to equation A2. At each trajectory time step t_n when the trajectory is in one of the target regions (AMA or CAR), $\Delta DU_{\mathrm{LAG}}(t_n)$ is added to the grid box where the trajectory started. This is done separately for the Amazon Basin and the Caribbean, and the resulting fields from all trajectories are shown in Figure 8.

For both target regions, the dominant dust-source regions are Mali, Mauritania, and Algeria. Dust reaching the Amazon Basin mainly originates from a belt, stretching from Central Algeria at 5°E/30°N to the eastern part of Mauritania at 10°W/20°N. Most of the dust reaching the Caribbean is also emitted from the central

21698996, 2015, 21, Downloaded from https://agupubs.onlinelibrary.wiley.com/doi/10.1002/2015JD023792 by Cochrane Czech Republic, Wiley Online Library on [01/05/2024]. See the Terms and Conditions (https://onlinelibrary.wiley.com/terms-and-conditions) on Wiley Online Library for rules of use; OA articles are governed by the applicable Creative Commons License

21698996, 2015, 21, Downloaded from https://agupubs.onlinelibrary.wiley.com/doi/10.1002/2015JD023792 by Cochrane Czech Republic, Wiley Online Library on [01/05/2024]. See the Terms and Conditions (https://onlinelibrary.wiley.com/terms-and-conditions) on Wiley Online Library for rules of use; OA articles are governed by the applicable Creative Commons License

Table 3. Dust Emission Fluxes and Dust Transport Along the Trajectories for Entire North Africa and the Arabian Peninsula, the Western Part of the Sahara, and the Bodélé Depression (See Figure 1 for Definition of the Regions)

	area	EMI_{EUL}	$EMI^{t_1}_{LAG}$	Share of EMI_{EUL}	$TRA^{30°W}_{LAG}$	Share of $EMI^{t_1}_{LAG}$
	10^6 km^2	Tg yr^{-1}	Tg yr^{-1}	%	Tg yr^{-1}	%
N Africa	23.19	1169.2	367.2	31	155.1	42
W Sahara	1.96	357.5	188.9	53	78.7	42
Bodélé Depression	0.38	125.2	26.1	21	1.4	5

and southwestern part of Algeria, with additional strong contributions from the northern and eastern part of Mauritania and northern Mali.

The dust emission hot spot in the Bodélé Depression (around 18°E/16°N) has been suggested to strongly contribute to the transatlantic dust transport, especially to the Amazon Basin during boreal winter [e.g., *Tegen et al.*, 2006; *Koren et al.*, 2006]. Figure 8, however, does not show any signal in this region, neither in DJF nor in JJA. Clearly, this obvious difference to earlier studies requires a more in-depth analysis and discussion.

6.2. Eulerian Approach

Three regions, i.e., entire North Africa, the western part of the Sahara (WSA) in Mali, Mauritania, and Algeria (10°W–5°E, 18–30°N), and the Bodélé Depression (15–20°E, 12–18°N), as marked in Figure 1a, are compared in Table 3. The integrated dust emission flux from entire North Africa is 1169.2 Tg yr^{-1}. About 30% therefrom originate from WSA (357.5 Tg yr^{-1}). The contribution of emissions from the Bodélé Depression is relatively high. Even though its area is only about one fifth of WSA, the emissions amount to 125.2 Tg yr^{-1}, which is 35% of the WSA value, demonstrating the outstanding importance of the Bodélé Depression as a general dust-source region. Figure 9 illustrates the time-lagged correlations between the time series of the emission fluxes and the transport across 30°W, for (a) emissions from WSA and (b) from the Bodélé Depression. Most seasons show distinct maxima in the correlations of the WSA time series for time shifts between 50 and 100 h, while there is no clear correlation peak visible for the Bodélé Depression. This purely Eulerian analysis confirms the Lagrangian finding that dust from the Bodélé Depression does not contribute to the dust that arrives in AMA or CAR. Most of this dust does not even reach 30°W.

6.3. Discussion

Integrating the fields shown in Figure 8 over North Africa results in the total dust deposition values given in Table 1, i.e., 11.4 Tg yr^{-1} in AMA (Figure 8a) and 13.8 Tg yr^{-1} in CAR (Figure 8b). Keeping in mind that these

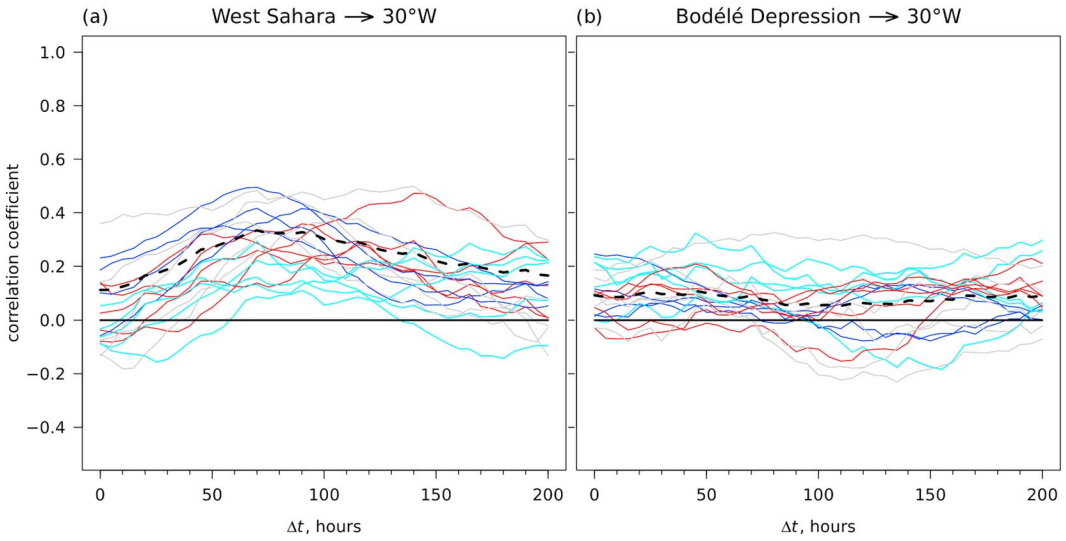

Figure 9. Time-lagged correlations of the normalized time series EMI_{EUL} and $TRA^{30°W}_{EUL}$ for dust emitted from (a) the western part of the Sahara and (b) the Bodélé Depression (see Figure 1 for definition of the regions). Solid lines show single seasons: DJF (blue), MAM (cyan), JJA (red), and SON (gray). Thick dashed black lines illustrate correlations for the time series of the entire 5 years.

Lagrangian values represent only about 40% of the Eulerian results (30.3 Tg yr^{-1} in AMA and 34.3 Tg yr^{-1} in CAR, see Table 1), these dust deposition fluxes are on the same order of magnitude as earlier values in literature (for AMA: 28 Tg yr^{-1} [*Yu et al.*, 2015], 40 Tg yr^{-1} [*Koren et al.*, 2006], and 50 ± 15 Tg yr^{-1} [*Kaufman et al.*, 2005]; for CAR: 50 ± 25 Tg yr^{-1} [*Kaufman et al.*, 2005]). The ability of EMAC to represent the transatlantic dust transport in a realistic way is again confirmed by this comparison.

Employing another dust emission scheme most probably would change the maps shown in Figure 8; would it also modify the role of the Bodélé Depression? Most emission schemes see this region as an emission hot spot in North Africa and worldwide [*Evan et al.*, 2015]. With the scheme by *Tegen et al.* [2002] that is employed in this study, absolute emission fluxes are highest in the grid boxes representing this emission hot spot [*Gläser et al.*, 2012; *Evan et al.*, 2015]. Therefore, it is unlikely that the missing signal of the Bodélé Depression results from too low emission there. One possible explanation for the discrepancies between the current and prior studies by *Kaufman et al.* [2005], *Tegen et al.* [2006], *Koren et al.* [2006], and *Ben-Ami et al.* [2012] — in addition to the very different methodologies — might be the fact that here we specifically focus on identifying the source regions for direct transatlantic dust transport. This means that dust emitted at one place, which sediments out of the considered trajectory during transport and is carried further by another air parcel, is not fully considered by our approach of trajectory selection (as discussed in section 4.1.2). This might potentially obscure the important role of some source regions, e.g., the Bodélé Depression, and require further Eulerian analyses.

$EMI^{t_1}_{LAG}$ in Table 3 lists the part of the Eulerian emission fluxes that is captured by the trajectories, initialized in the respective region. $TRA^{30°W}_{LAG}$ is the Lagrangian transport across 30°W. For entire North Africa, only 31% (367.2 Tg yr^{-1}) of the Eulerian emissions are represented by the trajectories, meaning that almost 70% of the dust is not transported across 30°W. This explains why there is no clear signal in the time-lagged correlations between EMI_{EUL} and TRA_{EUL} for the entire North Africa, as mentioned at the beginning of section 5.2. By contrast, for WSA, more than 50% (188.9 Tg yr^{-1}) are represented by the trajectories and 42% of this dust (78.7 Tg yr^{-1}) cross 30°W. Table 3 shows that only 21% (26.1 Tg yr^{-1}) of Eulerian dust emissions from the Bodélé Depression are captured by the trajectories. Of this very small amount, only 5% (1.4 Tg yr^{-1}) reach 30°W in the Lagrangian data. Altogether, both methods rule out the Bodélé Depression as an important source region for the transatlantic dust transport in our model data under year 2000 conditions, which is in contrast to earlier studies listed above.

While our simulation is too short to reach conclusions about the dust transport and its source regions on climatological time scales, there are some other recent studies doubting the importance of the Bodélé Depression for transatlantic dust transport. Based on the geochemical and isotopic composition of dust samples from various places in North Africa, Barbados, and the Amazon Basin, no obvious connection was found between dust from the Bodélé Depression and the transatlantic dust deposition samples [*Abouchami et al.*, 2013; *Pourmand et al.*, 2014], while samples from Mali, Niger, and Burkina Faso showed better agreement with those from Barbados [*Oldfield et al.*, 2014]. Measurements and trajectory analyses during the Saharan Aerosol Long-range Transport and Aerosol-Cloud interaction Experiment (SALTRACE) indicate that dust observed at Barbados often originates from Mali, Mauritania, and Algeria, and in a few cases also from the Bodélé Depression [*Groß et al.*, 2015]. *Scheuvens et al.* [2013] concluded from bulk compositional data of northern African dust that regions in the western Sahara, in particular, western Mauritania, southern Algeria, and northern Mali (defined as "potential source areas" PSA2 and PSA3) are the main contributors to the transatlantic dust transport. These regions match very well with the main source regions found in this model-based study, which are the deserts in central and southwest Algeria, Mauritania, and Mali (Figure 8).

Dust samples from Cape Verde do not show any characteristics of dust from the Bodélé Depression [*Groß et al.*, 2015]. Therefore, the question arises about the transport pathway of dust from this emission hot spot. To address this question, Figure 10 shows mean pathways and characteristics of trajectories starting from WSA and the Bodélé Depression, respectively. The highest mean dust mixing ratio along the trajectories of more than 2000 μg kg^{-1} is found for trajectories from the Bodélé Depression in DJF shortly after the emission (Figure 10a). These trajectories travel southwestward and stay below 850 hPa until they reach the Guinea coast, where they enter the ITCZ. Here the wet removal of dust is very effective (wet deposition contributes more than 70% to the total deposition flux), the dust mixing ratio decreases to less than 100 μg kg^{-1} between 5 and 10°W, and the trajectories have risen above 750 hPa. Trajectories starting from WSA travel many days at levels below 900 hPa in a dry tongue across the Atlantic, where the ratio of wet-to-total dust deposition is less than 50%. In these trajectories, the mean dust mixing ratio still accounts for about 200 μg kg^{-1} when crossing

21698996, 2015, 21, Downloaded from https://agupubs.onlinelibrary.wiley.com/doi/10.1002/2015JD023792 by Cochrane Czech Republic, Wiley Online Library on [01/05/2024]. See the Terms and Conditions (https://onlinelibrary.wiley.com/terms-and-conditions) on Wiley Online Library for rules of use; OA articles are governed by the applicable Creative Commons License

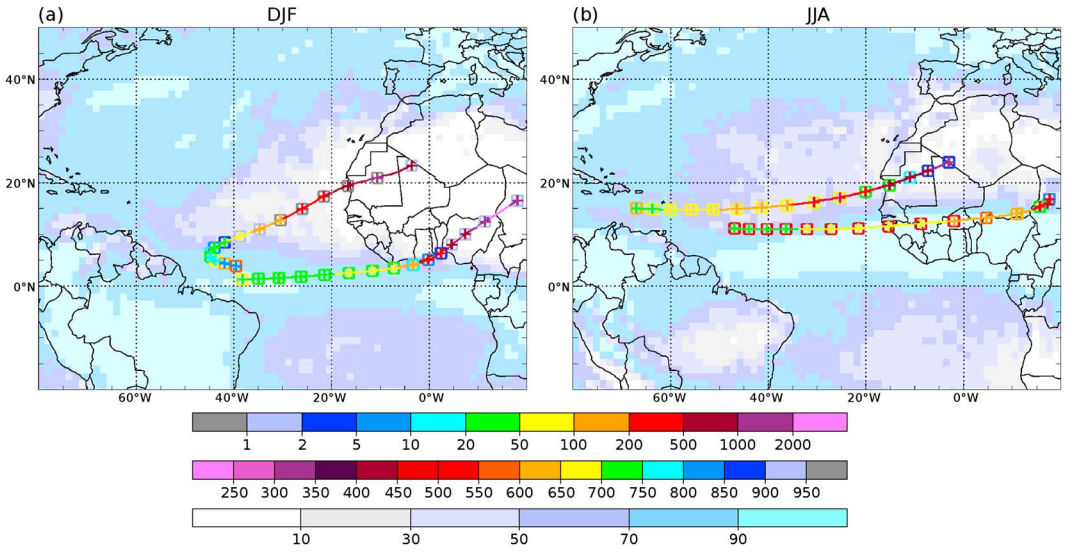

Figure 10. Mean pathways and characteristics of trajectories initialized in the western part of the Sahara and in the Bodélé Depression, respectively, during (a) DJF and (b) JJA. Symbols along the trajectories are drawn every 25 h (in compliance with the model and trajectory 5-hourly data output interval). Colored variables along the trajectories are the mean dust mixing ratio in μg kg^{-1} (upper colorbar, marked with "plus" symbols and shown along the connecting lines) and the mean pressure in hPa (middle colorbar, marked with "square" symbols). The underlying field shows the ratio of the Eulerian wet-to-total dust deposition flux in % (lower colorbar).

30°W. A similar behavior is visible in JJA (Figure 10b). The mean pathway of the Bodélé Depression trajectories encounters the ITCZ after 3 days, where the wet-to-total dust deposition ratio is higher than 90%. During that time, the air parcels ascend and the mean pressure decreases from 900 to 600 hPa. The westward transport then happens above 500 hPa with a quite low mean dust mixing ratio, which decreases to less than 100 μg kg^{-1} after 5 days. Again, the dust mixing ratio of trajectories from WSA stays above 100 μg kg^{-1} for about 10 days. On average, the transport from WSA occurs between 650 and 700 hPa, constituting the elevated SAL. These trajectories cross the Atlantic in a relatively dry region where wet deposition contributes less than 50% to the total deposition flux—as in DJF.

This first objectively determined Lagrangian connection between North African dust-source regions and the Americas, together with the Eulerian analyses, illustrates the importance of West African emission regions for the transatlantic transport of Saharan dust, while the Bodélé Depression plays only a minor role. Overall, the EMAC results presented here together with recent observations and geochemical analyses of dust samples reveal the complexity of determining detailed source maps of the transatlantic dust transport. *Cowie et al.* [2013] described a decreasing trend in dustiness over North Africa and the adjacent Atlantic Ocean since the 1980s. Such climatic and strong interannual variations [e.g., *Prospero and Lamb*, 2003] and the broad range of temporal and spatial scales involved in the dust cycle [*Shao et al.*, 2011] make us cautious in generalizing our results for very long climatic time scales. We cannot rule out that the Bodélé Depression contributes to the transatlantic dust transport under different climatic conditions.

7. Conclusions

On the basis of a previously evaluated 5 year time slice simulation of the global atmosphere-chemistry model EMAC [*Gläser et al.*, 2012], new findings on the transatlantic dust transport and its source regions are presented in this study. Eulerian and Lagrangian diagnostics and syntheses of both are used to investigate typical pathways and time scales of the transport of dust from North Africa to the Americas. Extensive trajectory analyses yield the first maps of the contribution of specific regions to the transatlantic dust transport in different seasons.

These maps identify central and southwestern Algeria, Mali, and Mauritania as the main source regions of dust crossing the Atlantic Ocean. Most of the dust deposited in both target regions, the Amazon Basin mainly during the boreal winter half year and the Caribbean during summer, was emitted from these regions in North Africa. Other deserts are neglected in this study as the dust transport to our target regions is predominated

21698996, 2015, 21, Downloaded from https://agupubs.onlinelibrary.wiley.com/doi/10.1002/2015JD023792 by Cochrane Czech Republic, Wiley Online Library on [01/05/2024]. See the Terms and Conditions (https://onlinelibrary.wiley.com/terms-and-conditions) on Wiley Online Library for rules of use; OA articles are governed by the applicable Creative Commons License

21698996, 2015, 21, Downloaded from https://agupubs.onlinelibrary.wiley.com/doi/10.1002/2015JD023792 by Cochrane Czech Republic, Wiley Online Library on [01/05/2024]. See the Terms and Conditions (https://onlinelibrary.wiley.com/terms-and-conditions) on Wiley Online Library for rules of use; OA articles are governed by the applicable Creative Commons License

from African sources [*Prospero et al.*, 2014]. In agreement with recent studies on the geochemical composition of dust deposited in Central and South America [*Oldfield et al.*, 2014; *Pourmand et al.*, 2014], the EMAC data suggest that dust from the Bodélé Depression plays only a minor role in the transatlantic transport. Trajectories starting in the Bodélé Depression enter the ITCZ before crossing the Atlantic leading to efficient wet removal of most of the dust before the air parcels reach the Americas. Composition and isotope analyses as the ones listed above and presented by *Abouchami et al.* [2013] and *Scheuvens et al.* [2013] could, in the future, focus on sites in the main contributing regions in central and southwest Algeria, Mauritania, and Mali (Figure 8) to experimentally validate our results by comparison with samples from South and Central America.

Furthermore, this study continues and extends the evaluation of the mineral dust cycle in EMAC by *Gläser et al.* [2012]. Well-known features of the transatlantic transport are reproduced by the model. The seasonality of horizontal and vertical structures is consistent with satellite data presented by *Liu et al.* [2012] and *Alizadeh-Choobari et al.* [2014]. The combination of Eulerian and Lagrangian diagnostics allows for a specification of the transport duration from the dust emission until rainout in the target areas. The resulting estimate for reaching the Caribbean in summer accounts to 280 h, i.e., 11 days and 16 h with an uncertainty range from 269 to 288 h. In winter, for the transport to AMA, our best estimate is exactly 10 days with an uncertainty range from 231 to 257 h. Large amounts of dust are typically transported on shorter time scales than the average dust transport. In addition, the analyses in this study show the highly episodic character of the transatlantic dust transport and deposition in the target regions—both can vary by 2 orders of magnitude on a daily time scale.

The comparison of Eulerian and Lagrangian results has shown that it is suitable to describe the transatlantic dust transport with a set of 15 day forward trajectories calculated from the dust emission grid points. Similar Lagrangian analyses with other simulations from other models, e.g., as those presented in *Kim et al.* [2014], would be an opportunity to test the robustness of our results on dust-source regions for transatlantic transport. The availability of well-established and tested diagnostic tools for analyzing the dust cycle and its source regions is also important to investigate the evolution of dust transport under changing climatic conditions as described by, e.g., *Nicholson et al.* [1998] and *Cowie et al.* [2013]. Variations in the hydroclimatology in the Sahel zone as happening, e.g., in the Niger River Basin due to climatic changes [*Oguntunde and Abiodun*, 2013] and direct human influences [*Descroix et al.*, 2012], might lead to shifts of the predominant source regions for the transatlantic dust transport. Estimates on the source strength of newly developing dust emission regions, and including them in transport studies like the one presented here, could provide insight into future characteristics of the transatlantic dust transport.

Appendix A: Details of the Lagrangian Setup

Different processes can cause increasing or decreasing dust mixing ratios along air parcel trajectories, in particular, turbulent entrainment of newly emitted dust in the boundary layer, wet and dry deposition, and numerical effects. These numerical effects include, e.g., errors in the offline trajectory computation and numerical diffusion of the dust concentration field in the Eulerian model. All these physical and numerical processes cause an exchange of dust from the trajectories considered here into air masses that are not captured by our trajectory setup, which leads to differences between the Eulerian and Lagrangian results, as discussed in section 4.1.2. The following detailed description of the Lagrangian diagnostics explains our measures to keep the discrepancies between both methodologies as small as possible.

A1. Weighting of the Trajectories

The initialization and selection of trajectories is schematically illustrated in Figure 1b. Depending on meteorological conditions, e.g., boundary layer stability, the dust emission flux is distributed rapidly in the vertical to all model levels in the planetary boundary layer. In order to be sure to capture all grid boxes in the vertical into which fresh dust is emitted, trajectories are initialized at each model layer from the surface (k_1) to the top of the planetary boundary layer (k_4 in Figure 1b), which is diagnosed in the model and available from model output. With this method, however, it cannot be distinguished between freshly emitted dust and earlier emitted dust that was transported into the considered grid box. This is an element of uncertainty that should be kept in mind for the comparison of Eulerian and Lagrangian results. To minimize double counting of dust with the trajectory approach, a weighting factor F_{EC} (the subscript *EC* refers to the dust *E*mission and *C*olumn mass) is

introduced for each grid point (i,j), which is mainly proportional to the Eulerian net dust emission flux and inversely proportional to the Eulerian boundary layer dust column mass. More precisely

$$F_{\mathrm{EC}}(i,j) = \begin{cases} 0, & \text{if } M_{\mathrm{emi}}(i,j) \le 0 \\ 1, & \text{if } M_{\mathrm{emi}}(i,j) \ge M_{\mathrm{bcol}}(i,j) \\ \frac{M_{\mathrm{emi}}(i,j)}{M_{\mathrm{bcol}}(i,j)}, & \text{else, with} \end{cases} \tag{A1}$$

$$M_{\mathrm{emi}}(i,j) = \Delta DU_{\mathrm{EUL}}(i,j) \cdot A(i,j) \cdot 18\,000\,\mathrm{s} \quad \text{and}$$

$$M_{\mathrm{bcol}}(i,j) = \sum_{k=1}^{k_{\max}} DU_{\mathrm{conc}}(i,j,k) \cdot V(i,j,k).$$

ΔDU_{EUL} denotes the Eulerian net dust emission flux, i.e., the difference of Eulerian mean dust emission minus deposition fluxes (in kg m^{-2} s^{-1}) during the last 5 h, i.e., one output time interval. To obtain the absolute Eulerian mass of dust emitted from the grid box during this time step, M_{emi}, the net emission flux is multiplied with the grid box area A and the 5 h time interval (= 18 000 s). M_{bcol} is the total mass of dust inside the boundary layer column at the grid point (i,j), calculated as the sum over all vertical levels from the surface ($k = 1$) to the planetary boundary layer height ($k = k_{\max}$) of the Eulerian dust concentration DU_{conc} times the volume V of grid box (i,j,k). If M_{emi} is less than 0, F_{EC} is set to 0, and if M_{bcol} is less than M_{emi}, then F_{EC} is set to 1, so that F_{EC} is defined in the range from 0 to 1. Weighting the trajectories with F_{EC} prevents double counting of dust that was emitted from grid box (i_1,j_1) at time t_1 and transported within the boundary layer into grid box (i_2,j_2) at time t_2. Without the weighting factor, this dust sample would be represented by a second trajectory, initialized at (i_2,j_2,t_2), even though the emission flux at (i_2,j_2) at time t_2 might be very small or even zero. F_{EC} also guarantees that trajectories initialized at grid points where the net dust emission flux is negative, i.e., where deposition exceeds emission, are not considered for the further analysis. All calculations based upon the trajectory data consider the weighting factor F_{EC}.

A2. Lagrangian Estimate of the Vertically Integrated Net Dust Gain

Here we describe the Lagrangian counterpart to the Eulerian net dust emission flux ΔDU_{EUL}. For every trajectory, the net dust gain is calculated as the material change of the dust mixing ratio (DU_{mix} in kgkg^{-1}) along the previous 5-hourly trajectory segment, multiplied with the trajectory mass m_T (in kg), which is constant along the trajectory. In the schematic example in Figure 1b, four trajectories are initialized above the brown grid point from the lowermost level (k_1) to the top of the planetary boundary layer (k_4 in this example). Since trajectory T_1 does not cross 30°W and, hence, is not considered a transatlantic transport trajectory, ΔDU_{LAG} of the blue grid point at time t is the sum of

$$\begin{aligned} &\left[DU_{\mathrm{mix}}(\mathrm{T}_2,t) - DU_{\mathrm{mix}}(\mathrm{T}_2,t-\Delta t)\right] \cdot m_T(\mathrm{T}_2) + \\ &\left[DU_{\mathrm{mix}}(\mathrm{T}_3,t) - DU_{\mathrm{mix}}(\mathrm{T}_3,t-\Delta t)\right] \cdot m_T(\mathrm{T}_3) + \\ &\left[DU_{\mathrm{mix}}(\mathrm{T}_4,t) - DU_{\mathrm{mix}}(\mathrm{T}_4,t-\Delta t)\right] \cdot m_T(\mathrm{T}_4) \quad , \end{aligned}$$

where $\Delta t = 5$ h is the model output time interval.

For the first trajectory time step (t_1), ΔDU_{LAG} is defined as the Eulerian value of emitted mass of dust, i.e., M_{emi} in equation (A1). Since there is no information about the vertical distribution of freshly emitted dust to the model levels inside the boundary layer, for simplicity, this mass is—for t_1 only—completely put to the lowermost trajectory that crosses 30°W (T_2 in Figure 1b).

Finally, for each grid point (i,j), seasonal values of ΔDU_{LAG} are calculated according to

$$\Delta DU^{X}_{\mathrm{LAG}}(i,j) = \sum_{\mathrm{T}_x \in X} \begin{cases} M_{\mathrm{emi}}(i,j,t_n) & \text{, if } n = 1 \\ \left(DU_{\mathrm{mix}}(t_n) - DU_{\mathrm{mix}}(t_{n-1})\right) \cdot m_{\mathrm{T}_x} & \text{, if } n > 1. \end{cases} \tag{A2}$$

$\mathrm{T}_x \in X$ defines all trajectories in the season X for X = DJF, MAM, JJA, and SON that fulfill the criterion that the trajectory coordinates at time step t_n are located within the grid box (i,j). The resulting fields are shown in section 4.1.

A3. Lagrangian Estimate of Zonal Dust Fluxes

The time integrated Lagrangian net zonal dust flux across a specific meridian, $\mathrm{TRA}_{\mathrm{LAG}}$, is calculated for every 5° latitude × 30 hPa height element of the considered vertical cross section. Therefore, DU_{mix} at the time

21698996, 2015, 21, Downloaded from https://agupubs.onlinelibrary.wiley.com/doi/10.1002/2015JD023792 by Cochrane Czech Republic, Wiley Online Library on [01/05/2024]. See the Terms and Conditions (https://onlinelibrary.wiley.com/terms-and-conditions) on Wiley Online Library for rules of use; OA articles are governed by the applicable Creative Commons License

when a trajectory T_x crosses the respective meridian is multiplied with m_{T_x} and divided by the area A of the latitude-height element it passes through.

$$\mathrm{TRA}_{\mathrm{LAG}} = \sum_{T_x \in X} \left(DU_{\mathrm{mix}} \cdot m_{T_x} \cdot \frac{1}{A} \right). \tag{A3}$$

Here the sum includes all trajectories crossing the considered latitude-height element during the season X. Trajectories crossing the meridians from west to east contribute with a negative flux to $\mathrm{TRA}_{\mathrm{LAG}}$. These zonal dust fluxes are shown in section 4.2.

Acknowledgments

All simulations were performed at the German Climate Computing Center (DKRZ) in Hamburg, Germany (project 507). The simulation results are archived on the CERA data server at DKRZ (http://cera-www.dkrz.de -experimentDKRZ_lta_507). ECHAM5/MESSy for Atmospheric Chemistry (EMAC) can be used by affiliates of member institutions of the MESSy consortium, which is open to all institutions signing the MESSy Memorandum of Understanding (http://www.messy-interface.org). The general circulation model ECHAM5 is made available by the Max Planck Institute for Meteorology, Hamburg, Germany (http://www.mpimet.mpg.de/en/science/models/echam.html). The trajectory tool LAGRANTO is publicly available and can be downloaded from www.lagranto.ethz.ch. This work was funded by the Research Centre Geocycles at the University of Mainz, and the authors got funding from the German Research Foundation within the project MACCHIATO (WE 2943/4-1) and the research unit PANDOWAE (FOR896) and from the MiKlip project (01 LP 1127 A) of the Federal Ministry of Education and Research of Germany. We are grateful to Patrick Jöckel (DLR) and the entire EMAC community for developing and assisting with using this sophisticated chemistry climate model. We would like to thank Peter Knippertz for fruitful discussions on dust emission and transport mechanisms. For their valuable comments, we are grateful to Jan-Berend Stuut, Owen Doherty, and one anonymous referee who helped to improve this paper.

References

Abouchami, W., et al. (2013), Geochemical and isotopic characterization of the Bodélé Depression dust source and implications for transatlantic dust transport to the Amazon Basin, *Earth Planet. Sci. Lett.*, *380*, 112–123, doi:10.1016/j.epsl.2013.08.028.

Adams, A. M., J. M. Prospero, and C. Zhang (2012), CALIPSO-derived three-dimensional structure of aerosol over the Atlantic basin and adjacent continents, *J. Clim.*, *25*(19), 6862–6879, doi:10.1175/JCLI-D-11-00672.1.

Alizadeh-Choobari, O., A. Sturman, and P. Zawar-Reza (2014), A global satellite view of the seasonal distribution of mineral dust and its correlation with atmospheric circulation, *Dyn. Atmos. Oceans*, *68*, 20–34, doi:10.1016/j.dynatmoce.2014.67.002.

Balkanski, Y., M. Schulz, T. Claquin, C. Moulin, and P. Ginoux (2004), Emission of atmospheric trace compounds, in *Global Emissions of Mineral Aerosol: Formulation and Validation Using satellite Imagery*, pp. 239–267, Kluwer Acad., Dordrecht, Netherlands.

Ben-Ami, Y., I. Koren, O. Altaratz, A. Kostinski, and Y. Lehahn (2012), Discernible rhythm in the spatio/temporal distributions of transatlantic dust, *Atmos. Chem. Phys.*, *12*(5), 2253–2262, doi:10.5194/acp-12-2253-2012.

Ben-Ami, Y., I. Koren, and O. Altaratz (2009), Patterns of North African dust transport over the Atlantic: Winter vs. summer, based on CALIPSO first year data, *Atmos. Chem. Phys.*, *9*(20), 7867–7875.

Bretl, S., P. Reutter, C. C. Raible, S. Ferrachat, C. S. Poberaj, L. E. Revell, and U. Lohmann (2015), The influence of absorbed solar radiation by Saharan dust on hurricane genesis, *J. Geophys. Res. Atmos.*, *120*, 1902–1917, doi:10.1002/2014JD022441.

Carlson, T. N., and J. M. Prospero (1972), The large-scale movement of Saharan air outbreaks over the northern equatorial Atlantic, *J. Appl. Meteorol.*, *11*(2), 283–297, doi:10.1175/1520-0450(1972)011<0283:TLSMOS>2.0.CO;2.

Chiapello, I., and C. Moulin (2002), TOMS and METEOSAT satellite records of the variability of Saharan dust transport over the Atlantic during the last two decades (1979–1997), *Geophys. Res. Lett.*, *29*(8), 17–1–17–4, doi:10.1029/2001GL013767.

Chiapello, I., C. Moulin, and J. M. Prospero (2005), Understanding the long-term variability of African dust transport across the Atlantic as recorded in both Barbados surface concentrations and large-scale Total Ozone Mapping Spectrometer (TOMS) optical thickness, *J. Geophys. Res.*, *110*, D18S10, doi:10.1029/2004JD005132.

Cowie, S. M., P. Knippertz, and J. H. Marsham (2013), Are vegetation-related roughness changes the cause of the recent decrease in dust emission from the Sahel?, *Geophys. Res. Lett.*, *40*, 1868–1872, doi:10.1002/grl.50273.

Cuesta, J., J. H. Marsham, D. J. Parker, and C. Flamant (2009), Dynamical mechanisms controlling the vertical redistribution of dust and the thermodynamic structure of the West Saharan atmospheric boundary layer during summer, *Atmos. Sci. Lett.*, *10*(1), 34–42, doi:10.1002/asl.207.

DeFlorio, M., I. Goodwin, D. Cayan, A. Miller, S. Ghan, D. Pierce, L. Russell, and B. Singh (2015), Interannual modulation of subtropical Atlantic boreal summer dust variability by ENSO, *Clim. Dyn.*, 1–15, doi:10.1007/s00382-015-2600-7.

DeFlorio, M. J., S. J. Ghan, B. Singh, A. J. Miller, D. R. Cayan, L. M. Russell, and R. C. J. Somerville (2014), Semidirect dynamical and radiative effect of North African dust transport on lower tropospheric clouds over the subtropical North Atlantic in CESM 1.0, *J. Geophys. Res. Atmos.*, *119*, 8284–8303, doi:10.1002/2013JD020997.

Descroix, L., P. Genthon, O. Amogu, J.-L. Rajot, D. Sighomnou, and M. Vauclin (2012), Change in Sahelian Rivers hydrograph: The case of recent red floods of the Niger River in the Niamey region, *Global Planet. Change*, *98–99*, 18–30, doi:10.1016/j.gloplacha.2012.07.009.

Doherty, O. M., N. Riemer, and S. Hameed (2008), Saharan mineral dust transport into the Caribbean: Observed atmospheric controls and trends, *J. Geophys. Res.*, *113*, D07211, doi:10.1029/2007JD009171.

Doherty, O. M., N. Riemer, and S. Hameed (2012), Control of Saharan mineral dust transport to Barbados in winter by the Intertropical Convergence Zone over West Africa, *J. Geophys. Res.*, *117*, D19117, doi:10.1029/2012JD017767.

Doherty, O. M., N. Riemer, and S. Hameed (2014), Role of the convergence zone over West Africa in controlling Saharan mineral dust load and transport in the boreal summer, *Tellus Ser. B*, *66*, 23191, doi:10.3402/tellusb.v66.23191.

Engelstaedter, S., and R. Washington (2007), Atmospheric controls on the annual cycle of North African dust, *J. Geophys. Res.*, *112*, D03103, doi:10.1029/2006JD007195.

Engelstaedter, S., I. Tegen, and R. Washington (2006), North African dust emissions and transport, *Earth Sci. Rev.*, *79*(1–2), 73–100, doi:10.1016/j.earscirev.2006.06.004.

Engelstaedter, S., R. Washington, and N. Mahowald (2009), Impact of changes in atmospheric conditions in modulating summer dust concentration at Barbados: A back-trajectory analysis, *J. Geophys. Res.*, *114*, D17111, doi:10.1029/2008JD011180.

Evan, A. T., A. K. Heidinger, and P. Knippertz (2006), Analysis of winter dust activity off the coast of West Africa using a new 24-year over-water advanced very high resolution radiometer satellite dust climatology, *J. Geophys. Res.*, *111*, D12210, doi:10.1029/2005JD006336.

Evan, A. T., S. Fiedler, C. Zhao, L. Menut, K. Schepanski, C. Flamant, and O. Doherty (2015), Derivation of an observation-based map of North African dust emission, *Aeolian Res.*, *16*, 153–162, doi:10.1016/j.aeolia.2015.01.001.

Fiedler, S., K. Schepanski, B. Heinold, P. Knippertz, and I. Tegen (2013), Climatology of nocturnal low-level jets over North Africa and implications for modeling mineral dust emission, *J. Geophys. Res. Atmos.*, *118*, 6100–6121, doi:10.1002/jgrd.50394.

Gläser, G., A. Kerkweg, and H. Wernli (2012), The mineral dust cycle in EMAC 2.40: Sensitivity to the spectral resolution and the dust emission scheme, *Atmos. Chem. Phys.*, *12*(3), 1611–1627, doi:10.5194/acp-12-1611-2012.

Gross, A., T. Goren, C. Pio, J. Cardoso, O. Tirosh, M. C. Todd, D. Rosenfeld, T. Weiner, D. Custodio, and A. Angert (2015), Variability in sources and concentrations of Saharan dust phosphorus over the Atlantic ocean, *Environ. Sci. Technol. Lett.*, *2*(2), 31–37, doi:10.1021/ez500399z.

Groß, S., V. Freudenthaler, K. Schepanski, C. Toledano, A. Schäfler, A. Ansmann, and B. Weinzierl (2015), Characterization of long-range transported Saharan dust at the Caribbean by dual-wavelength depolarization Raman lidar measurements, *Atmos. Chem. Phys. Discuss.*, *15*(13), 19,325–19,366, doi:10.5194/acpd-15-19325-2015.

21698996, 2015, 21, Downloaded from https://agupubs.onlinelibrary.wiley.com/doi/10.1002/2015JD023792 by Cochrane Czech Republic, Wiley Online Library on [01/05/2024]. See the Terms and Conditions (https://onlinelibrary.wiley.com/terms-and-conditions) on Wiley Online Library for rules of use; OA articles are governed by the applicable Creative Commons License

Heinold, B., P. Knippertz, J. H. Marsham, S. Fiedler, N. S. Dixon, K. Schepanski, B. Laurent, and I. Tegen (2013), The role of deep convection and nocturnal low-level jets for dust emission in summertime West Africa: Estimates from convection-permitting simulations, *J. Geophys. Res. Atmos.*, *118*, 4385–4400, doi:10.1002/jgrd.50402.

Hsu, S. C., et al. (2012), Dust transport from non-East Asian sources to the North Pacific, *Geophys. Res. Lett.*, *39*, L12804, doi:10.1029/2012GL051962.

Huneeus, N., et al. (2011), Global dust model intercomparison in AeroCom phase I, *Atmos. Chem. Phys.*, *11*(15), 7781–7816, doi:10.5194/acp-11-7781-2011.

Hunt, W. H., D. M. Winker, M. A. Vaughan, K. A. Powell, P. L. Lucker, and C. Weimer (2009), CALIPSO lidar description and performance assessment, *J. Atmos. Oceanic Technol.*, *26*(7), 1214–1228, doi:10.1175/2009JTECHA1223.1.

Jöckel, P., R. Sander, A. Kerkweg, H. Tost, and J. Lelieveld (2005), Technical note: The Modular Earth Submodel System (MESSy)—A new approach towards Earth System Modeling, *Atmos. Chem. Phys.*, *5*, 433–444.

Jöckel, P., A. Kerkweg, A. Pozzer, R. Sander, H. Tost, H. Riede, A. Baumgaertner, S. Gromov, and B. Kern (2010), Development cycle 2 of the Modular Earth Submodel System (MESSy2), *Geosci. Model Dev.*, *3*(2), 717–752, doi:10.5194/gmd-3-717-2010.

Junge, C. E. (1956), Recent investigations in air chemistry, *Tellus*, *8*(2), 127–139.

Karyampudi, V. M., et al. (1999), Validation of the Saharan dust plume conceptual model using lidar, Meteosat, and ECMWF data, *Bull. Am. Meteorol. Soc.*, *80*(6), 1045–1075, doi:10.1175/1520-0477(1999)080<1045:VOTSDP>2.0.CO;2.

Kaufman, Y. J., I. Koren, L. A. Remer, D. Tanré, P. Ginoux, and S. Fan (2005), Dust transport and deposition observed from the Terra-Moderate Resolution Imaging Spectroradiometer (MODIS) spacecraft over the Atlantic ocean, *J. Geophys. Res.*, *110*, D10S12, doi:10.1029/2003JD004436.

Kim, D., et al. (2014), Sources, sinks, and transatlantic transport of North African dust aerosol: A multimodel analysis and comparison with remote sensing data, *J. Geophys. Res. Atmos.*, *119*, 6259–6277, doi:10.1002/2013JD021099.

Knippertz, P., and J.-B. W. Stuut (eds.) (2014), *Mineral Dust—A Key Player in the Earth System*, 509 pp., Springer, Dordrecht, Netherlands.

Knippertz, P., and M. C. Todd (2012), Mineral dust aerosols over the Sahara: Meteorological controls on emission and transport and implications for modeling, *Rev. Geophys.*, *50*, RG1007, doi:10.1029/2011RG000362.

Koren, I., Y. J. Kaufman, R. Washington, M. C. Todd, Y. Rudich, J. V. Martins, and D. Rosenfeld (2006), The Bodélé depression: A single spot in the Sahara that provides most of the mineral dust to the Amazon forest, *Environ. Res. Lett.*, *1*(1), 014005, doi:10.1088/1748-9326/1/1/014005.

Liu, D., Y. J. Wang, Z. Wang, and J. Zhou (2012), The three-dimensional structure of transatlantic African dust transport: A new perspective from CALIPSO LIDAR measurements, *Adv. Meteorol.*, *2012*, 850704, doi:10.1155/2012/850704.

Mahowald, N., C. Luo, J. del Corral, and C. Zender (2003), Interannual variability in atmospheric mineral aerosols from a 22-year model simulation and observational data, *J. Geophys. Res.*, *108*(D12), 4352, doi:10.1029/2002JD002821.

Mahowald, N. M., A. R. Baker, G. Bergametti, N. Brooks, R. A. Duce, T. D. Jickells, N. Kubilay, J. M. Prospero, and I. Tegen (2005), Atmospheric global dust cycle and iron inputs to the ocean, *Global Biogeochem. Cycles*, *19*, GB4025, doi:10.1029/2004GB002402.

Mahowald, N. M., et al. (2010), Observed 20th century desert dust variability: Impact on climate and biogeochemistry, *Atmos. Chem. Phys.*, *10*(22), 10,875–10,893, doi:10.5194/acp-10-10875-2010.

McKendry, I. G., K. B. Strawbridge, N. T. O'Neill, A. M. Macdonald, P. S. K. Liu, W. R. Leaitch, K. G. Anlauf, L. Jaegle, T. D. Fairlie, and D. L. Westphal (2007), Trans-Pacific transport of Saharan dust to western North America: A case study, *J. Geophys. Res.*, *112*, D01103, doi:10.1029/2006JD007129.

Miller, R. L., et al. (2006), Mineral dust aerosols in the NASA Goddard Institute for Space Sciences ModelE atmospheric general circulation model, *J. Geophys. Res.*, *111*, D06208, doi:10.1029/2005JD005796.

Moulin, C., C. Lambert, F. Dulac, and U. Dayan (1997), Control of atmospheric export of dust from North Africa by the North Atlantic oscillation, *Nature*, *387*(6634), 691–694.

Mukhopadhyay, S., and P. Kreycik (2008), Dust generation and drought patterns in Africa from helium-4 in a modern Cape Verde coral, *Geophys. Res. Lett.*, *35*, L20820, doi:10.1029/2008GL035722.

Nicholson, S., C. Tucker, and M. Ba (1998), Desertification, drought, and surface vegetation: An example from the West African Sahel, *Bull. Am. Meteorol. Soc.*, *79*(5), 815–829, doi:10.1175/1520-0477(1998)079<0815:DDASVA>2.0.CO;2.

Nicholson, S. E. (2009), A revised picture of the structure of the "monsoon" and land ITCZ over West Africa, *Clim. Dyn.*, *32*(7–8), 1155–1171, doi:10.1007/s00382-008-0514-3.

Oguntunde, P. G., and B. J. Abiodun (2013), The impact of climate change on the Niger River Basin hydroclimatology, West Africa, *Clim. Dyn.*, *40*(1–2), 81–94, doi:10.1007/s00382-012-1498-6.

O'Hara, S. L., M. L. Clarke, and M. S. Elatrash (2006), Field measurements of desert dust deposition in Libya, *Atmos. Environ.*, *40*(21), 3881–3897, doi:10.1016/j.atmosenv.2006.02.020.

Oldfield, F., R. C. Chiverrell, R. Lyons, E. Williams, Z. Shen, C. Bristow, J. Bloemendal, J. Torrent, and J. F. Boyle (2014), Discriminating dusts and dusts sources using magnetic properties and hematite: Goethite ratios of surface materials and dust from North Africa, the Atlantic and Barbados, *Aeolian Res.*, *13*, 91–104, doi:10.1016/j.aeolia.2014.03.010.

Péwé, T. (Ed.) (1981), *Desert Dust: Origin, Characteristics, and Effect on Man*, 303 pp., Special paper - American Association for the Advancement of Science, Geol. Soc. of Am., Boulder, Colo.

Peyridieu, S., A. Chedin, D. Tanre, V. Capelle, C. Pierangelo, N. Lamquin, and R. Armante (2010), Saharan dust infrared optical depth and altitude retrieved from AIRS: A focus over North Atlantic - comparison to MODIS and CALIPSO, *Atmos. Chem. Phys.*, *10*(4), 1953–1967.

Pierangelo, C., A. Chédin, S. Heilliette, N. Jacquinet-Husson, and R. Armante (2004), Dust altitude and infrared optical depth from AIRS, *Atmos. Chem. Phys.*, *4*, 1813–1822.

Pourmand, A., J. M. Prospero, and A. Sharifi (2014), Geochemical fingerprinting of trans-Atlantic African dust based on radiogenic Sr-Nd-Hf isotopes and rare Earth element anomalies, *Geology*, *42*(8), 675–678, doi:10.1130/G35624.1.

Prenni, A. J., M. D. Petters, S. M. Kreidenweis, C. L. Heald, S. T. Martin, P. Artaxo, R. M. Garland, A. G. Wollny, and U. Pöschl (2009), Relative roles of biogenic emissions and Saharan dust as ice nuclei in the Amazon Basin, *Nat. Geosci.*, *2*(6), 401–404, doi:10.1038/NGEO517.

Prospero, J. (1999), Long-range transport of mineral dust in the global atmosphere: Impact of African dust on the environment of the southeastern United States, *Proc. Natl. Acad. Sci. U.S.A.*, *96*(7), 3396–3403, doi:10.1073/pnas.96.7.3396.

Prospero, J., and P. Lamb (2003), African droughts and dust transport to the Caribbean: Climate change implications, *Science*, *302*(5647), 1024–1027, doi:10.1126/science.1089915.

Prospero, J. M. (1999), Long-range transport of mineral dust in the global atmosphere: Impact of African dust on the environment of the southeastern United States, *Proc. Natl. Acad. Sci. U. S. A.*, *96*(7), 3396–3403, doi:10.1073/pnas.96.7.3396.

Prospero, J. M., and T. N. Carlson (1970), RADON-222 in North Atlantic trade winds. Its relationship to dust transport from Africa, *Science*, *167*(3920), 974–977, doi:10.1126/science.167.3920.974.

21698996, 2015, 21, Downloaded from https://agupubs.onlinelibrary.wiley.com/doi/10.1002/2015JD023792 by Cochrane Czech Republic, Wiley Online Library on [01/05/2024]. See the Terms and Conditions (https://onlinelibrary.wiley.com/terms-and-conditions) on Wiley Online Library for rules of use; OA articles are governed by the applicable Creative Commons License

Prospero, J. M., and R. T. Nees (1977), Dust concentration in atmosphere of equatorial North Atlantic—Possible relationship to Sahelian drought, *Science*, *196*(4295), 1196–1198, doi:10.1126/science.196.4295.1196.
Prospero, J. M., F.-X. Collard, J. Molinie, and A. Jeannot (2014), Characterizing the annual cycle of African dust transport to the Caribbean Basin and South America and its impact on the environment and air quality, *Global Biogeochem. Cycles*, *29*, 757–773, doi:10.1002/2013GB004802.
Roeckner, E., R. Brokopf, M. Esch, M. Giorgetta, S. Hagemann, L. Kornblueh, E. Manzini, U. Schlese, and U. Schulzweida (2006), Sensitivity of simulated climate to horizontal and vertical resolution in the ECHAM5 atmosphere model, *J. Clim.*, *19*(16), 3771–3791.
Schepanski, K., I. Tegen, and A. Macke (2009), Saharan dust transport and deposition towards the tropical northern Atlantic, *Atmos. Chem. Phys.*, *9*(4), 1173–1189.
Scheuvens, D., L. Schuetz, K. Kandler, M. Ebert, and S. Weinbruch (2013), Bulk composition of northern African dust and its source sediments—A compilation, *Earth Sci. Rev.*, *116*, 170–194, doi:10.1016/j.earscirev.2012.08.005.
Shao, Y., K.-H. Wyrwoll, A. Chappell, J. Huang, Z. Lin, G. H. McTainsh, M. Mikami, T. Y. Tanaka, X. Wang, and S. Yoon (2011), Dust cycle: An emerging core theme in Earth system science, *Aeolian Res.*, *2*(4), 181–204, doi:10.1016/j.aeolia.2011.02.001.
Sodemann, H., A. S. Palmer, C. Schwierz, M. Schwikowski, and H. Wernli (2006), The transport history of two Saharan dust events archived in an Alpine ice core, *Atmos. Chem. Phys.*, *6*, 667–688.
Stuut, J.-B. W., and M. A. Prins (2014), The significance of particle size of long-range transported mineral dust pages news, *PAGES News*, *22*(2), 14–15.
Swap, R., M. Garstang, S. Greco, R. Talbot, and P. Kallberg (1992), Saharan dust in the Amazon Basin, *Tellus Ser. B*, *44*(2), 133–149.
Tegen, I., B. Heinold, M. Todd, J. Helmert, R. Washington, and O. Dubovik (2006), Modelling soil dust aerosol in the Bodélé Depression during the BoDEx campaign, *Atmos. Chem. Phys.*, *6*, 4345–4359.
Tegen, I., S. P. Harrison, K. Kohfeld, I. C. Prentice, M. Coe, and M. Heimann (2002), Impact of vegetation and preferential source areas on global dust aerosol: Results from a model study, *J. Geophys. Res.*, *107*(D21), 4576, doi:10.1029/2001JD000963.
Trapp, J. M., F. J. Millero, and J. M. Prospero (2010), Temporal variability of the elemental composition of African dust measured in trade wind aerosols at Barbados and Miami, *Mar. Chem.*, *120*(1–4), 71–82, doi:10.1016/j.marchem.2008.10.004.
Varga, G., J. Kovacs, and G. Ujvari (2013), Analysis of Saharan dust intrusions into the Carpathian Basin (Central Europe) over the period of 1979–2011, *Global Planet. Change*, *100*, 333–342, doi:10.1016/j.gloplacha.2012.11.007.
Wang, S. H., N. C. Hsu, S. C. Tsay, N. H. Lin, A. M. Sayer, S. J. Huang, and W. K. M. Lau (2012), Can Asian dust trigger phytoplankton blooms in the oligotrophic northern South China Sea?, *Geophys. Res. Lett.*, *39*, L05811, doi:10.1029/2011GL050415.
Washington, R., C. Bouet, G. Cautenet, E. Mackenzie, I. Ashpole, S. Engelstaedter, G. Lizcano, G. M. Henderson, K. Schepanski, and I. Tegen (2009), Dust as a tipping element: The Bodélé Depression, Chad, *Proc. Natl. Acad. Sci. U.S.A.*, *106*(49), 20,564–20,571, doi:10.1073/pnas.0711850106.
Wernli, H., and H. C. Davies (1997), A Lagrangian-based analysis of extratropical cyclones. 1. The method and some applications, *Q. J. R. Meteorol. Soc.*, *123*(538, Part B), 467–489.
Wilks, D. S. (1995), *Statistical Methods in the Atmospheric Sciences*, 467 pp., Academic Press, San Diego, Calif.
Yu, H., et al. (2015), The fertilizing role of African dust in the Amazon rainforest: A first multiyear assessment based on data from Cloud-Aerosol Lidar and Infrared Pathfinder Satellite Observations, *Geophys. Res. Lett.*, *42*, 1984–1991, doi:10.1002/2015GL063040.

Erratum

In the originally published version of this article, several instances of text were incorrectly typeset. The following have since been corrected and this version may be considered the authoritative version of record. In the abstract, MEESy was changed to MESSy. Several instances of Bodele were changed to Bodélé.

21698996, 2015, 21, Downloaded from https://agupubs.onlinelibrary.wiley.com/doi/10.1002/2015JD023792 by Cochrane Czech Republic, Wiley Online Library on [01/05/2024]. See the Terms and Conditions (https://onlinelibrary.wiley.com/terms-and-conditions) on Wiley Online Library for rules of use; OA articles are governed by the applicable Creative Commons License